Interpretations of XeI and XeBr bound–free emission spectra and reactive quenching of Xe(3 P 2) atoms by bromine and iodine containing molecules

K. Tamagake, D. W. Setser, and J. H. Kolts

Citation: The Journal of Chemical Physics **74**, 4286 (1981); doi: 10.1063/1.441661
View online: http://dx.doi.org/10.1063/1.441661
View Table of Contents: http://scitation.aip.org/content/aip/journal/jcp/74/8?ver=pdfcov
Published by the AIP Publishing

Interpretations of XeI and XeBr bound-free emission spectra and reactive quenching of Xe($^3P_2$) atoms by bromine and iodine containing molecules

K. Tamagake

Faculty of Pharmaceutical Sciences, Okayama University, Okayama, Japan

D. W. Setser and J. H. Kolts

Department of Chemistry, Kansas State University, Manhattan, Kansas 66506

(Received 15 October 1980; accepted 26 December 1980)

The XeBr and XeI emissions spectra have been recorded in a flowing afterglow apparatus from the reaction of Xe($^3P_2$) atoms with 16 bromine and iodine containing reagents. In all cases both the B and C states of XeI and XeBr are observed; the inital B/C ratio is ~ 1.5. The ratio increase with pressure because of collisional transfer from C to B. Comparison of the total XeBr and XeI emission intensities with the XeCl emission intensity from Xe($^3P_2$) + Cl_2 is used to obtain rate constants for XeBr and XeI formation. The branching fractions for XeI and XeBr formation are large, probably unity, for Br_2, I_2, ICl, and IBr and relatively small for the polyatomic molecules except for CF_3I and possible CBr_4. From the short wavelength limit of the B–X spectra, upper limits to D_0(R–Br) and D_0(R–I) are assigned. The theoretical potential curves calculated by Dunning and Hay for the A, B, C, and X states of XeI and XeBr were slightly adjusted so that good agreement was obtained between the simulated and experimental spectra from low vibrational levels of the B and C states. These adjusted potential curves were used to simulate the spectra from high levels of XeBr and XeI, and initial XeBr and XeI vibrational distributions were assigned from matching the low pressure spectra. A systematic decrease in $\langle f_V(\mathrm{XeX})\rangle$ is observed in the Cl_2, Br_2, I_2 series and interpreted as evidence for X($^2P_{1/2}$) formation. The XeBr and XeI vibrational energy disposal is compared to that from reactions of metal atoms with halogen donors and with reactions of Xe($^3P_2$) with chlorine and fluorine donors.

I. INTRODUCTION

In previous work from this laboratory the bound-free rare gas halide emission spectra from reactions of metastable rare gas atoms with halogen containing molecules were used to assign rate constants for KrF* and XeF* formation,[1] develop the framework for simulating bound-free spectra using KrF* as an example,[2] and provide a detailed interpretation of the reaction dynamics for Xe($^3P_2$) reacting with a series of chlorine containing molecules.[3,4] In the present work the studies are extended to include the reactions of Xe($^3P_2$) with 16 bromine and iodine containing molecules:

$$\mathrm{Xe}(^3P_2)+\mathrm{RBr}\rightarrow \mathrm{XeBr}(B,\ 1/2)+\mathrm{R}\ , \tag{1a}$$

$$\rightarrow \mathrm{XeBr}(C,\ 3/2)+\mathrm{R}\ , \tag{1b}$$

$$\rightarrow \mathrm{XeBr}(D,\ 1/2)+\mathrm{R}\ ; \tag{1c}$$

$$\mathrm{Xe}(^3P_2)+\mathrm{RI}\rightarrow \mathrm{XeI}(B,\ 1/2)+\mathrm{R}\ , \tag{1d}$$

$$\rightarrow \mathrm{XeI}(C,\ 3/2)+\mathrm{R}\ , \tag{1e}$$

$$\rightarrow \mathrm{XeI}(D,\ 1/2)+\mathrm{R}\ . \tag{1f}$$

The XeI(D) and XeBr(D) states are formed only by the diatomic halogens, and even then in only a minor amount, and Reactions (1c) and (1f) will receive no further consideration. The Xe($^3P_2$) total quenching rate constants have been reported earlier,[5] and the present study is concerned with extracting information from the low pressure chemiluminescence XeBr and XeI spectra, which were obtained from the flowing afterglow technique. By comparing the XeBr and XeI emission intensities to the XeCl intensity from the Xe($^3P_2$) + Cl_2 reference reaction

$$\mathrm{Xe}(^3P_2)+\mathrm{Cl}_2\rightarrow \mathrm{XeCl}(B,\ C)+\mathrm{Cl}\ , \tag{2}$$

$$k_{\mathrm{XeCl}}=72\times10^{-11}\ \mathrm{cm}^3\,\mathrm{s}^{-1}\ ,\quad \Gamma_{\mathrm{XeCl}}=1.0\ ,$$

the formation rate constants k_{XeBr} and k_{XeI} were measured. Dividing these by the total quenching rate constant gives the branching fractions Γ_{XeBr} and Γ_{XeI}. By integrating the spectra over the proper ranges, with account taken of the XeBr and XeI(B, 1/2–A, 1/2) transition,[6,3] as well as the (B, 1/2–X, 1/2) transition, the formation ratio of the B and C states can be obtained. Since collisional transfer from the longer lived C state to the B state is rapid, low pressure data, ≤ 0.2 Torr of Ar, must be used to obtain spectra representing initial B/C ratios and initial vibrational distributions. Computer simulation of the XeI and XeBr spectra provide XeBr and XeI vibrational energy distributions for Reactions (1). The simulations do not include rotation and no information is obtained regarding rotational energy disposal. Within experimental uncertainty the product state distributions from the Xe($^3P_1$) reactions[7,8(a)] with halogen donors are the same as for Xe($^3P_2$), and the conclusions drawn here for Xe($^3P_2$) also apply to Xe($^3P_1$).

In principle, the energy ordering of the B and C states of XeBr and XeI can be obtained from high pressure B–X and C–A intensity ratios.[8] However, the necessary high pressure limit can not be reached in our flowing afterglow apparatus and other techniques are needed.[8(a)] For XeF and XeCl the C state is[8] lower than the B state by ~700 and ~200 cm^{-1}, respectively. The two XeBr states[8(c),8(d)] are very close together and the

0021-9606/81/084286-20$01.00

XeI(B) state may be below the C state. Overlapping (C–A) and (B–A) bands and uncertain τ_B/τ_C ratios make assignment of the state ordering from the emission intensity ratios especially difficult for XeBr and XeI. In the present work emphasis is on the low pressure data; the high pressure results and the energy ordering question will be discussed later.[8(c)]

The computational techniques that were developed for the KrF simulations were employed for XeBr and XeI. Before successful spectral simulations can be done, accurate potential curves must be adopted. For the XeF(B–X) and XeCl(B–X) simulations[3,4] a flat lower potential and essentially a Rittner upper potential were used. However, for KrF the repulsive wall of the lower potential was important[2] and this also is expected for XeBr and XeI. The present calculations include a realistic ground state potential and the variation of the transition moment with internuclear distance. The B–X transition was used to assign the vibrational distributions. For XeI the B–X, B–A, and C–A transitions are well separated and simulations were done for the B–A and C–A transitions in order to gain information about the shapes of the lower state potentials. Unfortunately, the B–A and C–A transitions of XeBr are badly overlapped, which makes the B–A simulation of little value and reduces the usefulness of the C–A simulation too. The HBr and HI reactions give rare gas halide molecules in low vibrational levels, which are useful distributions for deducing potential curves. Golde and Kvaran[9] recently obtained ArBr potentials by simulating the ArBr spectra from Ar($^3P_{0,2}$) + HBr. The spectra from Xe($^3P_2$) + HBr and HI were heavily weighted in assigning the XeBr and XeI potential curves.

The dynamical interpretations that could be drawn from the XeCl and XeF results[3,7] were restricted somewhat because most detailed studies of alkali and alkaline earth metal atom reactions have been with bromides and iodides rather than with chlorides.[10] Where comparisons could be made, a close correspondence in vibrational energy disposal between Xe* + RCl and the analogous metal atom reaction seemed to exist.[7,10] Iodides and bromide reagents were selected to maximize the comparisons that could be made with former metal atom studies. For polyatomic halides, Γ_{XeI} or Γ_{XeBr} tend to be small for inorganic or organic halogen donors; however, even with this limitation several series could still be selected for comparison. Several interesting features were found which have not been reported from metal atom studies. One is that $\langle f_V(\mathrm{XeX})\rangle$ declines in the halogen family: $F_2 \approx Cl_2 > Br_2 > I_2$. The trends in vibrational energy disposal from Xe($^3P_2$) and metal atom reactions with polyatomic halide donors are similar; however, $\langle f_V(\mathrm{XeX})\rangle$ usually is less than $\langle f_V(\mathrm{MX})\rangle$. These differences are *tentatively* associated with the presence of multiple potentials in the exist channel for Xe($^3P_2$) or Xe($^3P_1$) atom reactions.

II. EXPERIMENTAL TECHNIQUES

Two flowing afterglow reactors[3] were used to obtain XeBr and XeI emission spectra from the Xe($^3P_2$) + RBr and RI reactions. One was used to obtain spectra from 0.1 to 0.5 Torr, and the other for measuring product formation rate constants and obtaining spectra from 0.5 to ~50 Torr. Total quenching rate constants have been reported previously[5] and will not be discussed here. Both flow reactors were of the coaxial mixing type (the rare gas flows through the inner tube and the reagent through the outer tube). Metastable Xe atoms were generated by adding a small flow of Xe(~40 μmol min^{-1}) to the main Ar flow (90 mmol min^{-1}). The combined rare gas flows passed through rolled tantalum foil electrodes (~0.7 cm diam. and separated by ~1 cm) operated at 200 to 250 V, depending on the pressure. The high pressure reactor (>0.5 Torr) was pumped by a 1000 ℓ min^{-1} mechanical pump. The low pressure reactor (<0.5 Torr) was pumped by a small Roots type blower and mechanical pump with a combined pumping capacity of ~3000 ℓ min^{-1}. The reactor used on the higher pressure apparatus was separated from the discharge by a right angle bend which included a Woods' horn light trap. In order to reduce loss of Xe($^3P_2$) by diffusion in the low pressure reactor, the right angle bend was eliminated so that the distance separating the electrodes and mixing region was as short as possible. The Xe($^3P_0$) and Ar($^3P_2$) concentrations were below the detection limit of atomic absorption spectroscopy. Typical Xe($^3P_2$) concentrations were 10^{11}–10^{10} atom cm^{-3}. Effects, if any, introduced by the elimination of the light trap in the low pressure reactor were negligible, as shown by the exact match of spectra obtained in the high and low pressure reactors at the same pressures. The most likely difference would be the presence of Xe($^3P_1$) atoms in the low pressure reactor. However, the Xe($^3P_1$) reactions with halogen donors closely resemble[7,8(a)] those of Xe($^3P_2$) and, even if some Xe($^3P_1$) atoms were present, little difference would be expected.

The XeBr and XeI emission spectra were observed through a Spectrosil quartz window that was attached (by epoxy) to the mixing zone of the Pyrex glass reactor. The spectra were recorded with a 0.75 m Jarrell-Ash scanning monochromator with a cooled E.M.I, 9558 photomultiplier tube and SSR photon counter. The spectral response of the detection train was carefully calibrated from 190 to 340 nm using a standard D_2 lamp (Optronic Labs) and by a quartz–iodine lamp (Electro Optics Associates) from 300 to 830 nm. The monochromator and photomultiplier output were interfaced to a PDP/8E computer that controlled scanning and data acquisition.[11] After the actual experiment was completed, the data were corrected for spectral response; integration or plotting was done with the computer. All spectra shown in this paper have been corrected for wavelength response.

Reagents were handled in different ways depending upon the vapor pressure. For reagents with vapor pressure ≥5 Torr at room temperature, the samples were prepared by diluting the purified reagent gas with argon to produce a 5% to 15% mixture and stored in Pyrex bulbs. For reagents which are decomposed by room light, the mixtures were prepared the same day of the experiment and stored in blackened bulbs. Reagent flows from the reservoirs were measured from the pressure change in a standard volume as a function of time. Re-

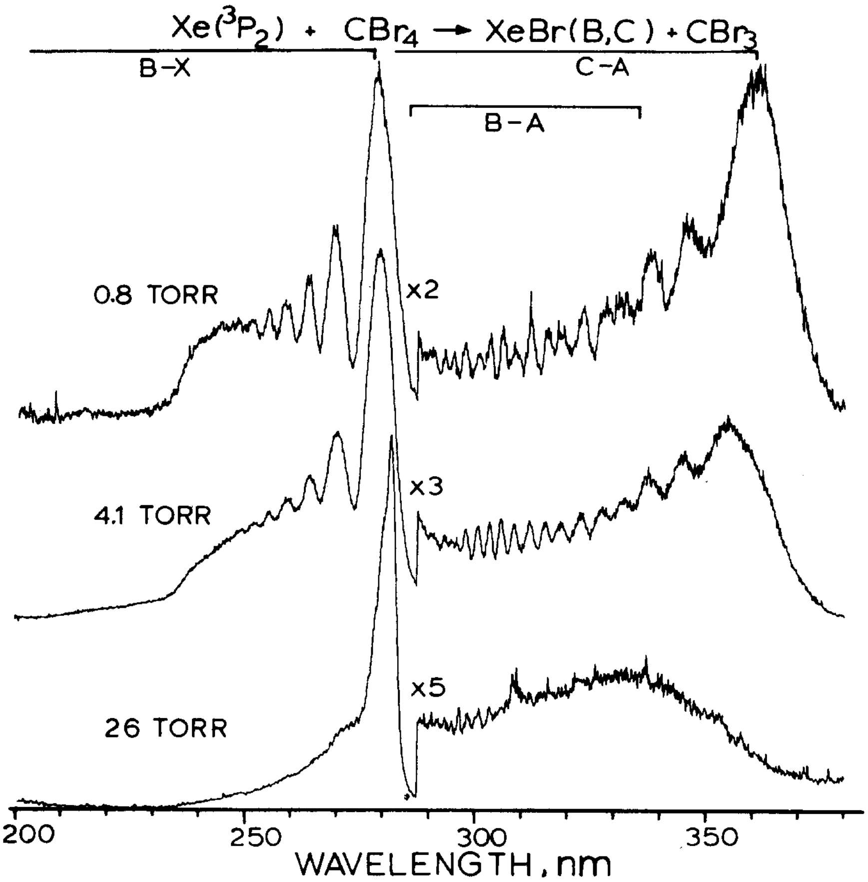

FIG. 1. XeBr chemiluminescence spectra from Xe($^3P_2$)+CBr$_4$ at 0.81, 4.1, and 25.7 Torr of Ar. The S/N ratio is low for the 0.8 Torr spectrum, but, emission does extend to 203 nm following the abrupt drop in intensity at ~240 nm. This is more apparent in the 4.1 Torr spectrum. The C–A and B–A bands are badly overlapped (see text).

agents with low vapor pressures were added to the flowing afterglow by placing the reagent in a 3 cm diameter tube and passing a small flow of argon over the sample; the concentrations were controlled by the argon flow rate and/or by the temperature of the sample. For the low vapor pressure samples, the reagent flow rates were not quantitatively measured and hence k_{XeBr} or k_{XeI} could not be determined. All portions of the vaccum system that were in contact with RBr of RI reagents were Pyrex glass; stopcocks were of the glass–Teflon type. Gaseous reagents were obtained from Matheson lecture bottles; the liquid and solid reagents were the standard grades from commercial suppliers except for SF$_5$Br, which was synthesized from the reaction of S$_2$F$_{10}$ with BR$_2$. All reagents were vacuum distilled prior to use.

III. EXPERIMENTAL RESULTS

A. General spectral features of XeBr and XeI

The reactions of Xe($^3P_2$) with Br$_2$ and I$_2$ gave weak Br_2^* and I_2^* emission which overlap the XeBr and XeI spectra to some extent. Therefore, in order to display the characteristic chemiluminescence spectra from highly vibrationally excited XeI and XeBr molecules, the spectra from CBr$_4$ and CF$_3$I are shown in Figs. 1 and 2, respectively, at three pressures. The low pressure XeI spectrum shows three resolved band systems: (B, 1/2–X, 1/2) 190–256 nm, (B, 1/2–A, 1/2) 301–340 nm, and (C, 3/2–A, 3/2) 256–301 nm. As the pressure is increased, these bands change in intensity, position,

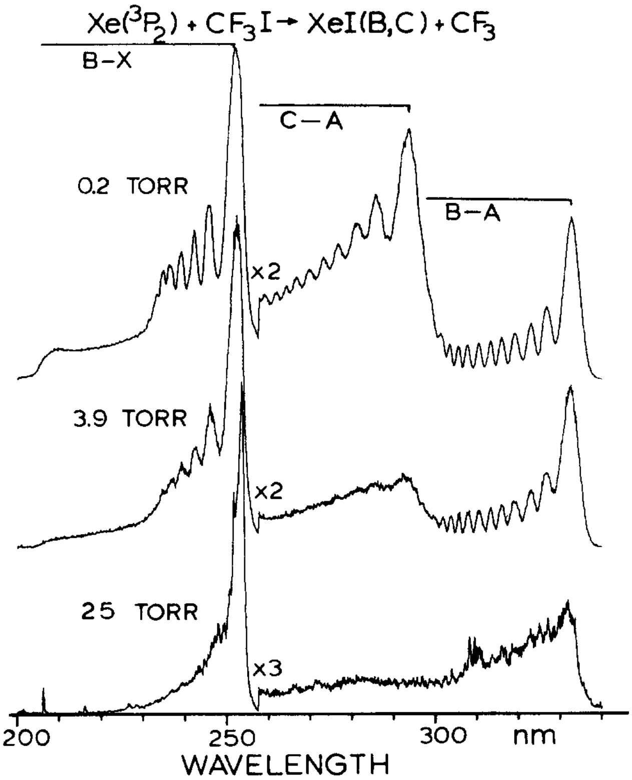

FIG. 2. XeI chemiluminescence spectra from Xe($^3P_2$)+CF$_3$I at 0.22, 3.9, and 25.2 Torr of Ar. The drop in intensity at ~202 nm corresponds to the thermochemical limit for this reaction.

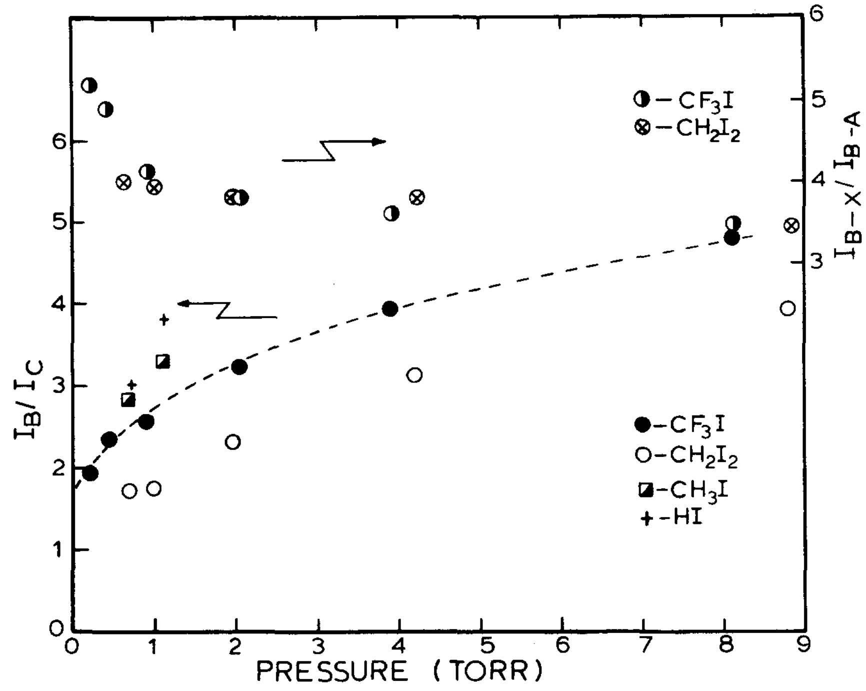

FIG. 3. Pressure dependence of the XeI(B–X, A)/XeI(C–A) intensity (lower plot) and XeI(B–X)/XeI(B–A) ratios (upper plot). The dotted curve was drawn through the CF$_3$I points to indicate how zero pressure extrapolations were made to obtain I_B/I_C. The I_B/I_C ratio continues to slowly increase beyond 10 Torr and is six and five for CF$_3$I and CH$_2$I$_2$, respectively, at 25 Torr. The I_{B-X}/I_{B-A} ratios from HI and CH$_3$I, which are not shown were ~2, rather than ~3.5. The reduction is expected for lower vibrational distributions, but background emission may contribute more to the apparent B–A emission for these weak emission intensities.

and shape and it becomes more difficult to clearly define the three bands. However, the low pressure CF$_3$I spectra is particularly well resolved and assignment is very clear cut. For the I$_2$ reaction, a small XeI(D, 1/2–X, 1/2) contribution also is evident at 202.5 nm, but this emission is not observed from CF$_3$I. The XeBr(B, 1/2–X, 1/2) transition is well resolved and lies between 203–285 nm for the CBr$_4$ reaction. The 285–380 nm region contains overlapping XeBr(B, 1/2–A, 1/2) and XeBr(C, 3/2–A, 3/2) bands. In contrast to XeI, the redmost broad XeBr band probably is the (C–A) transition; the more closely spaced oscillations in the 290–320 nm region are assigned to the B–A transition. The B–A band tends to maintain this oscillatory pattern more than the C–A emission as the pressure is increased. The calculated[6] B–X/B–A branching ratio is 3.5, 4.1, and 15.5 for XeI, XeBr, and XeCl, respectively. For XeCl the B–A emission is sufficiently weak that it can be effectively ignored, and for XeI the B–X and B–A bands are resolved and each can be measured. The radiative branching from the B state causes difficulty in interpretation only for XeBr. An overview of the XeBr emission from various donors is shown in Fig. 5.

Increasing pressure reduces the relative importance of the C–A emission and also dampens out the oscillations in the spectra. The former is a consequence of C–B collisional transfer and the latter from vibrational relaxation. In order to assign reliable initial vibrational distributions, spectra obtained at ≤ 0.2 Torr of Ar are required for simulation. However, the initial B/C state ratio may be estimated by extrapolation of data from 0.5–5 Torr to zero pressure. The variation of $I_{B-A,X}/I_{C-A}$ is shown in Fig. 3 for several iodide donors. Extrapolation to zero pressure gives the initial XeI B/C ratios in Table II. The I_{B-X}/I_{B-A} ratio, shown in Fig. 3, varies significantly with pressure and with donor, i.e., the branching fraction is dependent upon vibrational excitation. At 10 Torr the ratio is ~3.4 for CF$_3$I and CH$_2$I$_2$. Above 50 Torr[8(c)] the vibrational distribution is nearly 300 K Boltzmann and the I_{B-X}/I_{B-A} ratio has declined to 1.6 ± 0.2, which can be compared to the calculated value[6] of 3.5.

The initial XeBr(B)/XeBr(C) ratios must be assigned differently from the XeI case because of the overlapping B–A and C–A transitions. First, the ratio of I(B–X)/I(B–μ)+I(C–A) was plotted versus pressure and extrapolated to zero pressure (see Fig. 4). This ratio was then converted to the initial I_B/I_C ratio by using the measured XeBr(B–X) intensity and the calculated I_{B-X}/I_{B-A} ratio. Based upon the comparison of XeI data with the calculations, this method of correction should be a good approximation.

The compilation in Table I shows that each reaction yields both B and C states with B being somewhat more highly favored. This is a general trend for all halogen donors except PCl$_3$, which gave more XeCl(C) than XeCl(B). For some reactions, the spectra were obtained only at 0.5 Torr. For such cases the initial B/C ratio was estimated by analogy to the extrapolated curves shown in Figs. 3 and 4.

The short wavelength limit of the rare gas halide emission can be used to set upper limits to D_0(R–X).[1,3] The relationship for XeBr(B) can be written as

$$D_0(\mathrm{R{-}Br}) \leq E(\mathrm{Xe},\ {}^3P_2) + nRT - E_{\lambda\min}[\mathrm{XeBr}(B{-}X)]\ , \tag{3}$$

assuming that the activation barrier to reaction can be taken as zero. The nRT term accounts for the contribution of thermal energy to the collision. If only translational and rotational energy contribute to the available energy, $n = 5/2$ and 3 for diatomic and polyatomic reagents, respectively. Although the *envelope* of the

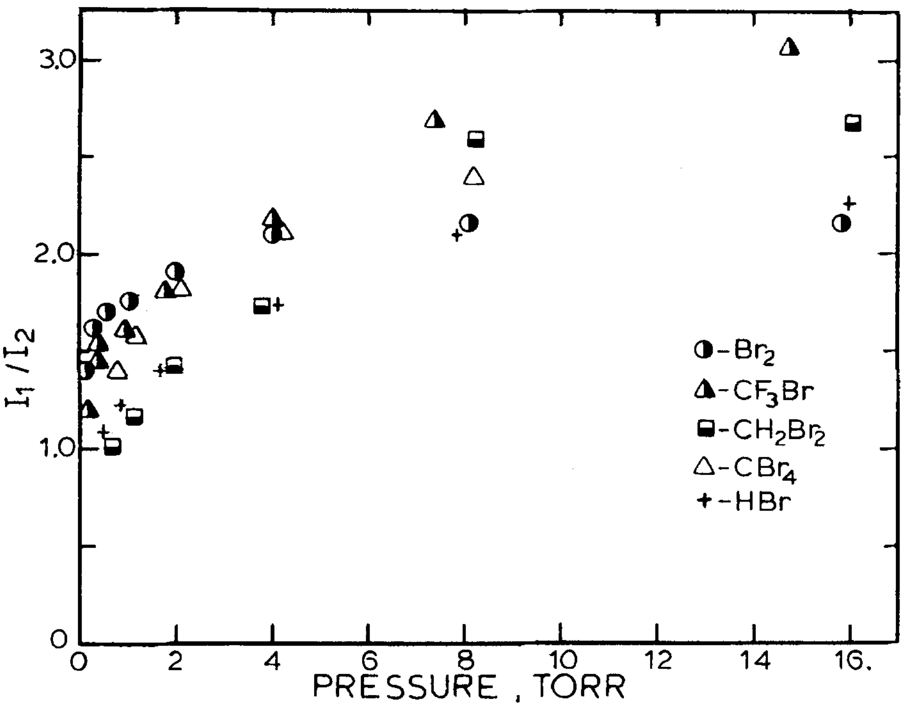

FIG. 4. Pressure dependence of the XeBr(B–X)/XeBr(C–A) + XeBr(B–A) emission intensity ratio. This ratio I_1/I_2 was extrapolated to zero pressure and then corrected for the XeBr(B–A) contribution to get the initial B/C ratios given in Table I (see text).

B–X band is sensitive to the shape of the lower potential, *vide infra*, the short wavelength *limit* still measures the energy of the highest populated XeBr level, providing that the transition at the outer turning point terminates at $V_X(R) \approx 0$. This requirement is satisfied for moderate vibrational excitation. Equation (3) necessarily is an upper limit to D_0(R–Br) because the reaction may not yield XeBr(B) in the highest level permitted by the available energy. A corollary to Eq. (3) provides the highest observed vibrational energy $E^{\rm obs}_{v\max}$ from a given B–X spectrum:

$$E^{\rm obs}_{v\max} = \nu_{\max} - [\nu_0 + V_X(R_e')] = \nu_{\max} - T_e \ , \qquad (4)$$

where $\nu_{\max} = \lambda^{-1}_{\min}$, ν_0 is the band origin, and $V_X(R_e)$ is the lower state potential energy at R_e'. Relations similar to Eqs. (3) and (4) hold for XeI. The D_0(R–X) and $E^{\rm obs}_{v\max}$ values derived from the B–X spectra are tabulated in Table II.

Except for I_2 for which $\lambda_{\min} < 190$ nm, the short wavelength limit is between 230–195 nm. In this range the response of the detection system is falling; therefore, there is greater uncertainty in the $\lambda_{\min}$ values for XeBr and XeI than for XeCl[3] or XeF[1]. The chemical purity of the iodide and bromide samples also can be a problem, even though precautions were taken. For the molecular halogens, other than I_2 for which $\lambda_{\min}$ was not observed, there is a good correspondence between the known bond energy and the upper limit deduced from the B–X emission spectra. There is no strong evidence that another RT of energy should be added to Eq. (3) to account for vibrational energy of the reactant. For reactions with significant $\Gamma_{X\bullet X}$, the XeBr(B–X) or XeI(B–X) short wavelength limit provides a relatively good measure of the bond energy, and values given in Table I for CF_3–I, PBr_2–Br, and $CHBr_2$–Br should be reliable limits. As would be expected from the analogous findings from metal atom reactions, the vibrational energy release was low for Xe($^3P_2$) + CH_3Br and CH_2Br_2 and the $\lambda_{\min}$ values do not provide good lower limits to the bond energies in these cases. Unfortunately, window contamination and a very small sample combined to make the SF_5Br experiment of only qualitative value. The true D_0(Br–SF_5) probably is significantly less than 50 kcal mol^{-1}. Hydrogen iodide and hydrogen bromide are special cases because $E^{\rm obs}_{v\max}$ is so small. For HI the branching fraction for XeI formation is relatively high (see Table I) and $\lambda_{\min}$ is consistent with D_0(H–I). The HBr reaction is the only one for which the derived bond energy is below the literature value by more than the combined experimental uncertainties. Since D_0(H–Br) is well established, perhaps the higher energy component of the Boltzmann distribution mainly is responsible for XeBr formation. This would be consistent with the low branching fraction for Xe($^3P_2$) + HBr. One must be careful to eliminate Br_2 or I_2 impurity from HBr and HI, respectively. However, Br_2 definitely was not in the sample used to obtain the HBr spectrum, as can be ascertained by comparing the XeBr spectra from the two reactions (see Fig. 5).

B. Assignment of rate constants and branching fractions

The total quenching rate constants have been measured[5] for about one half of the molecules in Table I. For the others, quenching rate constants can be estimated reliably in either of two ways. If the thermal cross section has been measured for Ar($^3P_2$), the value for Xe($^3P_2$) can be estimated[5] as ~1.4 times larger. This was done for CH_3Br and CH_3I using the k_Q(Ar, $^3P_2$) values.[16] Alternatively, if a series of k_Q values are known, the linear correlation of σ_Q with C_6 coefficient[5] can be used to estimate σ_Q for new reagents. All of the molecules

TABLE I. Rate constants, branching fractions, and B/C ratios.

Reagent	k_Q (10^{-11} cm^3 s^{-1})	k_{XeX^*}	Γ_{XeX}	$(B/C)^g$	$(B/C)_{p=0}{}^h$
I_2	d	e	0.8 $\Gamma_{I_2^*} = 0.2$		~1.8
HI	40^a	6.2	0.16	2.8	1.8
CF_3I	52^a	19.7	0.38	1.9	1.7
CH_3I	123^a	1.1	~0.01	2.8	1.8
CH_2I_2	151^c	not measured, but > 0.1 some I_2^* emission			~1.8
ICl	50^a	e	$\Gamma_{XeCl} = 0.70$ $\Gamma_{XeI} = 0.30$		
IBr	~70^a	e	$\Gamma_{XeBr} = 0.67$ $\Gamma_{XeI} = 0.33$ Γ_{IBr^*} = trace		
Br_2	60^a	63^f	0.98 $\Gamma_{Br_2^*} = 0.02$	2.6	1.6
HBr	61^a	$\gtrsim 5$	$\gtrsim 0.08$	1.7	1.2
CF_3Br	42^a	6	0.14	2.1	1.4
CH_3Br	77^b	trace	< 0.01		
CH_2Br_2	91^c	1.3	0.014	1.7	1.2
$CHBr_3$	114^c		not measured, but > 0.1	2.0	1.2
CBr_4	125^c		not measured, but > 0.1	2.6	1.3
PBr_3	120^c	9.3	~0.08	1.6	1.2
SF_5Br	80^c	5.7	$\lesssim 0.07$	1.9	1.4

[a] Obtained from Ref. 5; the magnitude of the rate constants for HBr and HI seem to be inverted and some experimental error is suspected. The value for IBr was taken to be the same as for Kr($^3P_2$).

[b] Obtained from the Ar($^3P_2$) quenching rate constant, Ref. 11(a), by scaling the cross sections with the C_6 coefficients.

[c] Estimated from dependence of cross section upon C_6 coefficient or polarizability; the CH_3Br and CH_3I rate constants for Ar($^3P_2$) were used as absolute references.

[d] k_Q was obtained from the Cs + I_2 cross section, since the low vapor pressure prevented reliable metering of I_2.

[e] For these cases k_{XeI} or k_{XeBr} were not measured because of difficulties encountered in gas handling. Since the emission was quite strong, it was assumed that quenching gives only XeX*.

[f] This is the rate constant for all emissions, including both XeBr and Br_2^*.

[g] These values for both XeBr and XeI are for the lowest experimentally observed pressure, which is 0.5–1.0 Torr, except for Br_2, CF_3Br, and CF_3I which was 0.10 Torr. The B/C ratio for XeI was directly measured from the separated B–X, B–A, and C–A bands (but, see Sec. IV D). The XeBr(B)/XeBr(C) ratio was obtained from the [I(B–X) + I(B–A)]/I(C–A) ratio using the calculated I(B–X)/I(B–A) ratio (see text).

[h] These are the ratios obtained by graphical extrapolation of the preceding column to the zero pressure limit (see Figs. 2 and 3).

in Table I are expected to have large rate constants and the estimated values should be good to ± 30%.

The XeBr and XeI formation rate constants were measured with the reference reaction technique in the same way as those for XeCl* formation.[3] For the same concentration of Xe($^3P_2$) atoms the integrated XeCl and XeBr of XeI emission intensities from Xe($^3P_2$) + Cl_2 and from Xe($^3P_2$) + RBr or RI were measured. Equation (5) with $k_{XeCl} = 72 \times 10^{-11}$ cm^3 s^{-1} gives k_{XeBr^*} and a similar relation holds for k_{XeI^*}:

$$k_{XeBr} = \frac{I_{XeBr}/[RBr]}{I_{XeCl}/[Cl_2]} k_{XeCl^*} . \quad (5)$$

The branching fractions are k_{XeBr^*}/k_Q .

Because of either low vapor pressure or chemical instability, some reagent flow rates were not metered reliably. For I_2, IBr, and ICl the emission intensity is strong and all of the quenching was assumed to give light emission; the relative emission intensities were assigned as the branching fractions. Flow rates were

TABLE II. Bond energies from $(B-X)$ short wavelength limits.

		Bond energy (kcal mol^{-1})		$E_{V\max}$ (kcal mol^{-1})	
Reagent	$\lambda_{\min}^{\text{obs}}$ (nm)	Exptl[a]	Literature[b]	Obs[d]	Thermochem[c]
I_2	< 187.0	< 40.3	35.60 ± 0.01	> 38.8	43.5
HI	233.0	70.5	70.4 ± 0.1	8.8	8.7
CF_3I	202.0	52.0	53.2 ± 2[e]	27.4	26.2
CH_3I	223.0	65.3	55.7 ± 0.3[f]	14.1	23.7
CH_2I_2	205.0	54.0	50.3 ± 2[f]	25.4	29.1
ICl(XeI)	~ 200(XeI)	~ 50.2	49.7 ± 0.1	28.9	29.4
IBr	192.5(XeI)	44.7	42.5 ± 0.1	34.4	36.6
Br_2	194.0	45.8	45.45 ± 0.01	45.3	45.6
HBr	263–264	84.5–84.9	86.6 ± 0.1	6.6–6.3	4.5
CF_3Br	228.0	68.1	68.7 ± 2[e,g]	23.3	22.7
CH_3Br	not reliable	···	69 ± 2[g]	···	22.4
CH_2Br_2	236.0	72.3	61 ± 3	19.1	30.4
$CHBr_3$	214.0	59.9	~ 56	31.5	~ 35
CBr_4	203.0	52.7	49 ± 3	38.8	42.4
PBr_3	215	60.5	···	30.9	···
SF_5Br	~ 215[b]	< 60.5[h]	···	≤ 30.9[h]	···

[a] Obtained from Eq. (3); these are upper limit values (see text).

[b] Taken from Ref. 12 unless specified otherwise.

[c] Available maximum vibrational energy calculated as $E_{V\max}^{\text{Th}} = E(\text{Xe})^* + nRT - D_0(\text{R-Br}) - [\nu_0 + V_X(R_e')]$ (see footnote d).

[d] Maximum vibrational energies deduced from $\lambda_{\min}^{\text{obs}}$ using Eq. (4), $\{E_{V\max}^{\text{obs}} = \nu_{\max} - [\nu_0 + V_X(R_e')]\}$, or $\nu_{\max} - T_e$, where $\nu_{\max}$ is $1/\lambda_{\min}^{\text{obs}}$, ν_0 is band origin, e.g., 35453 and 39553 cm^{-1} for XeBr and XeI, respectively. $V_X(R_e')$ was obtained from the dispersion-corrected *ab initio* potential (Table IV) and is 245 and 347 cm^{-1} for XeBr and XeI, respectively. $E_{\max}^{\text{obs}}$ are lower limits to the maximum vibrational energy, $E_{V\max}^{\text{Th}}$.

[e] Taken from Ref. 13.

[f] Taken from Ref. 14.

[g] Taken from Ref. 15.

[h] Lack of sample prevented the measurement of a reliable limit.

not measured for CH_2I_2, $CHBr_3$, and CBr_4 because of their low vapor pressures; although the emission was relatively strong, the unit branching fraction assumption is not justified for these polyatomic cases.[7]

The only emission observed, other than from XeI or XeBr, for reactions in Table I were I_2^*(345 and 280 nm), Br_2^*(291 nm), and IBr**(385 nm). These are commonly observed continuum emissions associated with the transition from the ionic halogen state to weakly bound states of intermediate energy. Generally, $\Gamma_{X_2^*}$ increases with increasing energy of the metastable atom and atomic number of X_2.[7] For example, $\Gamma_{Br_2^*} = 0.25$ for Kr($^3P_2$) + Br_2 and 0.2 for Xe($^3P_2$) + I_2.

The Γ_{XeBr} and Γ_{XeI} are consistent with the general trends from the fluoride and chloride donors[1-3,7] in that only molecular halogens have branching fractions approaching unity. The bromine or iodine compounds analogous to the fluorine and chlorine polyatomic molecules with high branching fractions, such as OF_2, NF_3, SCl_2, and OCl_2, are not sufficiently stable to be studied. Fortunately, several of the carbon compounds (CBr_4, CH_2I_2, CF_3I, and CF_3Br) are moderately good donors. The branching fraction for XeX* formation steadily increases, as does the exoergicity, for the HCl, HBr, and HI series.

IV. SPECTRAL ANALYSIS AND SIMULATION

A. Preliminary analysis of $B-X$ bands

The maximum thermochemical and observed vibrational energies are listed in Table II. The actual average vibrational energy $\langle E_V \rangle$ or most probable vibrational energy E_{mp} were first estimated from the spacings of the oscillatory structure in the $B-X$ bands of XeBr by using Eq. (12) of Ref. 2 with $\omega_e'[\text{XeBr}(B)] = 120$ cm^{-1}. This ω_e' was assigned by Tellinghuisen[17(a)] from simulation of a high pressure XeBr spectrum assuming a 300 K Boltzmann population. However, the resulting E_{mp} values (38 and 49 kcal mol^{-1} for CBr_4 and Br_2, respectively) seemed unreasonably high judging from the $E_{V\max}^{\text{obs}}$ in Table II. This means $\omega_e' = 120$ cm^{-1} is too low for XeBr(B). If we assume $f_{\text{mp}} = E_{\text{mp}}/E_{V\max}^{\text{obs}} = 0.7-0.9$ by analogy to Xe* + CCl_4 or Cl_2, the lower limit to ω_e'(XeBr)

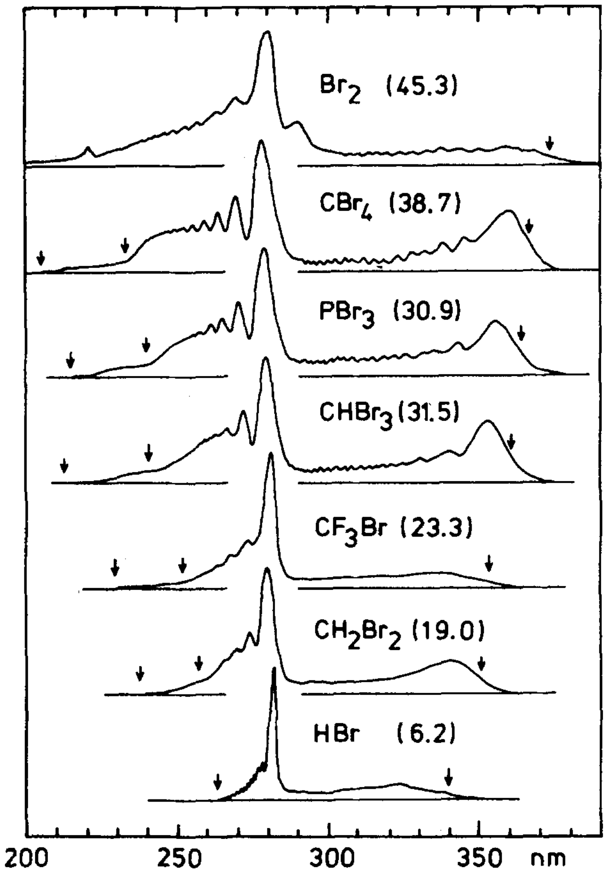

FIG. 5. XeBr emission from Xe($^3P_2$) plus various RBr reagents at ≤ 0.5 Torr Ar pressure. The $E^{\rm obs}_{V\max}$ values are shown in parenthesis. The arrows on the short wavelength side denote $\lambda_{\min}$; the center arrows show the positions λ_B where the intensity drops rather abruptly in the B–X transition. The arrows on the red side show λ_B for the B–A or C–A transitions. The band at 290 nm in the Xe($^3P_2$) + Br$_2$ spectrum is a Br$_2^*$ emission.

must be 130 cm^{-1}. The *ab initio* calculation of Hay and Dunning[6] gave $\omega_e' = 133$ cm^{-1}, which is consistent with the above statement. A similar analysis of the XeI(B–X) spectrum from Xe + CF$_3$I suggests that ω_e'[XeI(B)] = 120 cm^{-1}, whereas Tellinghuisen *et al.*[17(a)] recommended 112 cm^{-1}. One explanation[17(b)] of this discrepancy is that the spectra used for simulation by Ref. 17(a) were not completely vibrationally relaxed.

Preliminary simulations (all calculations were done using the NEAC ACOS-70 computer at Okayama University) for XeBr were done using the *ab initio* potential for the upper state and a flat lower potential. The resulting vibrational distributions, determined mainly by the oscillatory behavior of the spectrum, were quite reasonable and close to the final results obtained with a modified lower potential, as will be described in detail hereafter. However, the overall envelope of the computed spectra did not match the experimental spectra. In particular, the sudden decrease of intensity observed (see Fig. 5) at 240 nm for CBr$_4$ and at 246 nm for CHBr$_3$ was not reproduced. A similar drop in intensity occurs for the XeI spectra (at 230 nm in the CF$_3$I spectrum) and even in the XeCl spectrum from Xe* + CCl$_4$,[4] although it is less obvious for the latter. Since the wavelength for the sudden drop in intensity varies with reagent (or the vibrational energy in the upper state) and since the simulated spectra from a flat lower potential never shows such appearance, the drop must be due to the termination of B-type transitions at long wavelength because of the repulsive wall in the lower state. The A-type transitions extend to shorter wavelength, but the variation of the transition moment with R strongly discriminates against those transitions. The terms A-type and B-type transition denote the classical transitions at the outer and inner turning point of the potential, respectively, as defined in Ref. 2. The location of

TABLE III. Wavlengths (nm) of characteristic points used to examine the lower potentials.

		B–X			C–A		B–A	
		λ_A [a]	λ_B [a]	λ_0	λ_0	λ_B [b]	λ_0	λ_B [d]
XeBr	Br$_2$	194	(not clear)				(369)[c]	
	CBr$_4$	202	232 nm				(368)[c]	
	PBr$_3$	315	240				(364)[c]	
	CHBr$_3$	220	242				(361)[c]	
	CF$_3$Br	228	(252)				(354)[c]	
	CH$_2$Br$_2$	236	(258)				(351)[c]	
	HBr	263					(340)[c]	
	high pressure			282 nm		~300 nm	325 nm	
XeI	I$_2$	< 187	(not clear)			300		335
	CF$_3$I	203	229			297		335
	CH$_2$I$_2$	307	232			296		335
	CH$_3$I	223	243			288		232
	HI	233				283		331
	high pressure			253 nm	263 ± 3 nm		320 ± 5 nm	

[a] These wavelengths correspond to the short wavelength limit and to the point of abrupt drop in intensity of the B–X band (see Fig. 5).

[b] These wavelengths correspond to the positions where the intensity declines by about 50% from the maximum of the redmost band of the C–A transition (see Fig. 5).

[c] These wavelengths probably correspond to the C–A transition, but see text.

[d] These wavelengths correspond to the position of the long wavelength maximum of the B–A band.

TABLE IV. *Ab initio* and dispersion-corrected potentials.[a]

State	T_e[b] (cm^{-1})	A (cm^{-1})	B (10^7 cm^{-1})	C (cm^{-1} Å^{-1})	D_1 (10^5 cm^{-1} Å)	D_4 (10^5 cm^{-1} Å)	D_6 (10^6 cm^{-1} Å^6)	R_e[c] (Å)	ω_e'[c] (cm^{-1})
XeBr									
ab initio									
(B, 1/2)	37 058(36 314)	33 289	2.1554	2.3496	1.1614	8.6057	0	3.3817	129.3
(A, 1/2)	3685	0	5.9110	3.0099	0	0	0		
(X, 1/2)	0	0	3.8064	3.1546	0	0	0		
(C, 3/2)	37 583(36 839)	30 400	2.5806	2.4780	1.0191	8.0255	0	3.3158	130.7
(A, 3/2)	0	0	5.5280	2.9469	0	0	0		
dispersion-corrected									
(B, 1/2)	36 759(35 698)	33 588	2.1554	2.3496	1.1614	8.6057	0.439	3.3603	130.6
(A, 1/2)	3633	52	5.9110	3.0099	0	0	1.012	4.742	
(X, 1/2)	−122	122	3.8064	3.1546	0	0	1.012	4.049	
(C, 3/2)	37 246(36 185)	30 737	2.5806	2.4780	1.0191	8.0255	0.439	3.2917	132.3
(A, 3/2)	−44	44	5.5280	2.9469	0	0	1.012	4.883	
XeI									
ab initio[c]									
(B, 1/2)	40 211(40 612)	30 897	3.5408	2.4414	1.1799	5.9058	0	3.6076	105.2
(A, 1/2)	7 601	0	8.7471	2.9593	0	0	0		
(X, 1/2)	0	0	5.7912	3.0171	0	0	0		
(C, 3/2)	40 928(41 329)	30 482	5.6303	2.7145	1.2096	0.1349	0	3.5636	103.9
(A, 3/2)	0	0	5.1117	2.7415	0	0	0		
dispersion-corrected									
(B, 1/2)	39 919(39 900)	31 188	3.5408	2.4414	1.1799	5.9058	0.63	3.5850	106.5
(A, 1/2)	7519	82	8.7471	2.9593	0	0	1.73	4.795	
(X, 1/2)	−140	140	5.7912	3.0171	0	0	1.73	4.343	
(C, 3/2)	40 614(40 595)	30 797	5.6303	2.7145	1.2096	0.1349	0.63	3.5383	105.5
(A, 3/2)	−55	55	5.1117	2.7415	0	0	1.73	5.119	

[a] The (X, 1/2) state energy at $R=\infty$ was set equal to zero; $V(R)=T_e+A+B\exp(-CR)-D_1/R-D_4/R^4-D_6/R^6$.

[b] Minimum value of the potential. The values in parenthesis are the values adjusted so that the origin of the B–X band could be matched to the observed one.

[c] Values calculated with the parameters may not be exactly the same as the original values given by Hay and Dunning since these parameters were obtained by least-squares fitting. The polarizabilities (ionization energies) for Xe, Xe$^+$, Br, Br$^-$, I, and I$^-$ are 3.99(12.13), 3.0(21.2), 3.5(11.84), 4.17(3.36), 6.37(10.45), and 6.44(3.06), respectively; the units are Å^3 and eV.

these transitions is indicated by the arrows in the XeBr(B–X) spectra shown in Fig. 5 and the wavelengths are listed in Table III. Evaluations of these two characteristic type transitions defines the lower potential, since the difference between ν_A and ν_B (frequencies of A-type and B-type transitions, respectively) measure the difference in potential energy at the two different internuclear distances in the lower state corresponding to the turning points in the upper state. These values depend upon the mean excitation energy in the B state, and the ν_A and ν_B values for different reagents give information about the lower state for a range of R.

B. Modifications of the *ab initio* potentials and transition moments

Before undertaking complete simulations, examination of the *ab initio*[8] potentials and transition moments was necessary. The *ab initio* upper state potentials were fitted to Rittner type functions by a least-square method; the parameters of Eq. (6) are listed in Table IV:

$$V(R) = T_e + A + B\exp(-CR) - D_1/R - D_4/R^4 . \qquad (6)$$

Here T_e is the minimum value of $V(R)$ and A is the dissociation energy. The B–X spectra computed with these potentials and the preliminary vibrational distributions showed an intensity drop in the midspectral region. However, the drop occurred at longer wavelength than in the real spectrum. This means that the *ab initio* lower potential is too steep with respect to the upper potential. In order to see this more clearly, $\nu_A - \nu_B$ was plotted against $\nu_A - \nu_0$, where ν_0 is the frequency of the vertical transition from the equilibrium position in the upper state (see Fig. 6). The sharp peak at 282 (253) nm in the high pressure spectra of XeBr(XeI) was assigned to ν_0. As we see from Fig. 6, the *ab initio* potentials tend to overestimate $\nu_A - \nu_B$ by 20%–30% for both XeBr and XeI.

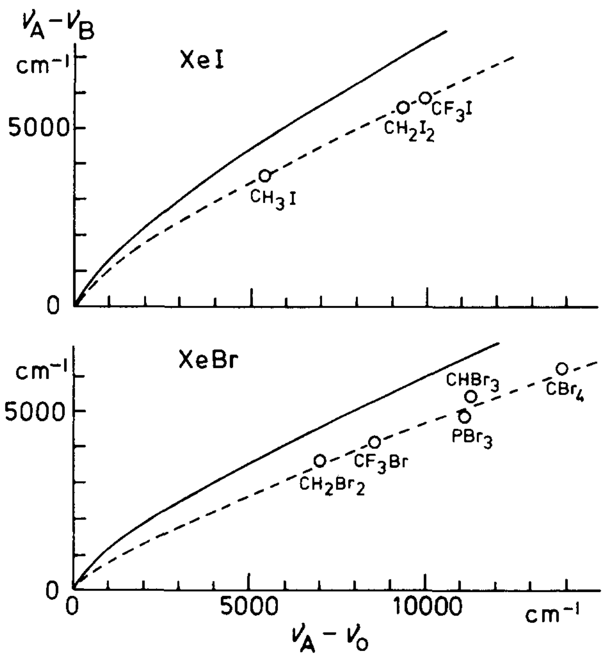

FIG. 6. Plots of $\nu_A - \nu_B$ vs $\nu_A - \nu_0$ for XeBr(B–X) and XeI(B–X) spectra. The points are experimental data; the solid and dotted curves are the calculated results from the *ab initio* and dispersion-corrected *ab initio* potentials, respectively.

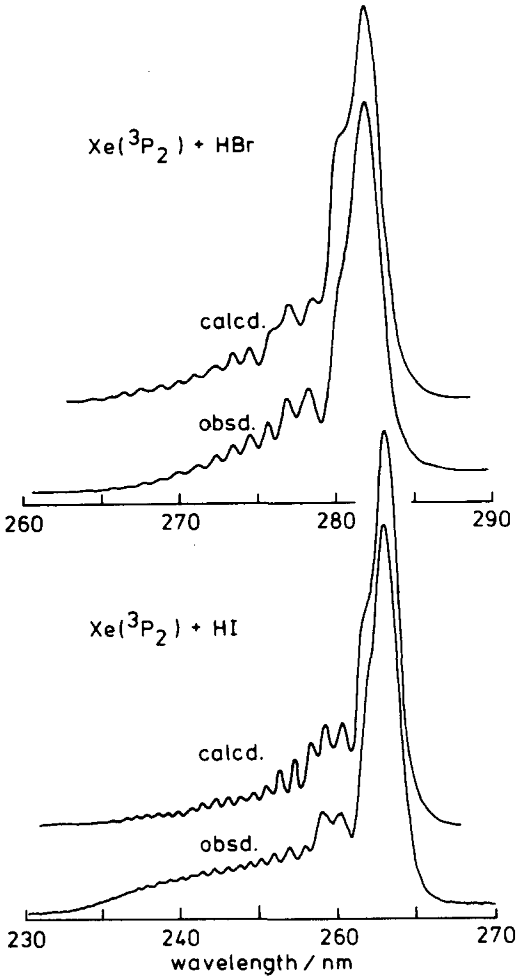

FIG. 7. Comparison of calculated and experimental XeBr and XeI chemiluminescence spectra from Xe($^3P_2$) + HBr (0.5 Torr) and HI (1.0 Torr), respectively.

The repulsive walls of the *ab initio* KrF(X) and XeCl(X) potentials also were found to be too steep relative to the real case.[2,4] This partly is a consequence of underestimation of the dispersion forced by the *ab initio* calculations. Therefore, a term

$$V_{\mathrm{disp}} = \tfrac{3}{2}\,\alpha_1\,\alpha_2 \left(\frac{V_1 V_2}{V_1 + V_2}\right) \Big/ R^6 \qquad (7)$$

was added to the *ab initio* potential, and the dispersion-corrected, *ab initio* potentials give good agreement with the observed $\nu_A - \nu_B$ values as shown by the broken line in Fig. 6.

The $\nu_A - \nu_B$ plot was convenient for checking the relative shapes of the upper and lower repulsive potentials, but gives no information about ω_e' and $\omega_e x_e'$. The fine structure in the Xe($^3P_2$) + HBr spectrum provides good information for ω_e' of XeBr(B, 1/2) since the spectrum shows A-type transitions from $v' \leq 12$ levels (see Fig. 5). Using the anharmonicity of the dispersion corrected *ab initio* potential and $\omega_e' = 143 \pm 2$ cm^{-1} reproduced the positions of the peaks in the Xe($^3P_2$) + HBr spectrum (see Fig. 7). The spectroscopic parameters needed for

TABLE V. Spectroscopic parameters for $(B,1/2)$ and $(X,1/2)$ states.[a]

	XeBr	XeI
ω_e'	143 cm^{-1}	122 cm^{-1}
$\omega_e x_e'$	0.343 cm^{-1}	0.276 cm^{-1}
$V_B(R_e')-V_X(R_e')$	35430 cm^{-1}	39500 cm^{-1}
$V_X(R_e')-V_X(\infty)$	268 cm^{-1}	400 cm^{-1}
$V_X(R_e'')-V_X(\infty)$	-133 cm^{-1}	-160 cm^{-1}
$(dV_X/dR)_{R_e'}$	-1990 cm^{-1}/Å	-2290 cm^{-1}/Å
$(d^2V_X/dR^2)_{R_e'}$	7468 cm^{-1}/Å^2	9060 cm^{-1}/Å^2

[a] These values were obtained from the best fit to the XeBr and XeI spectra from the HBr and HI reactions; both scales of the abscissa and the ordinate of the dispersion corrected potentials in Table III were changed according to Eq. (17) in Ref. 2. These These are slightly different from the values deduced from the "final potentials" described in the text. Computations showed the values in this table were better for Xe($^3P_2$)+HBr and Xe($^3P_2$)+HI+spectra. However, for spectra from other reactions there was no significant improvement in the fit using these parameters vs the best values of Table III.

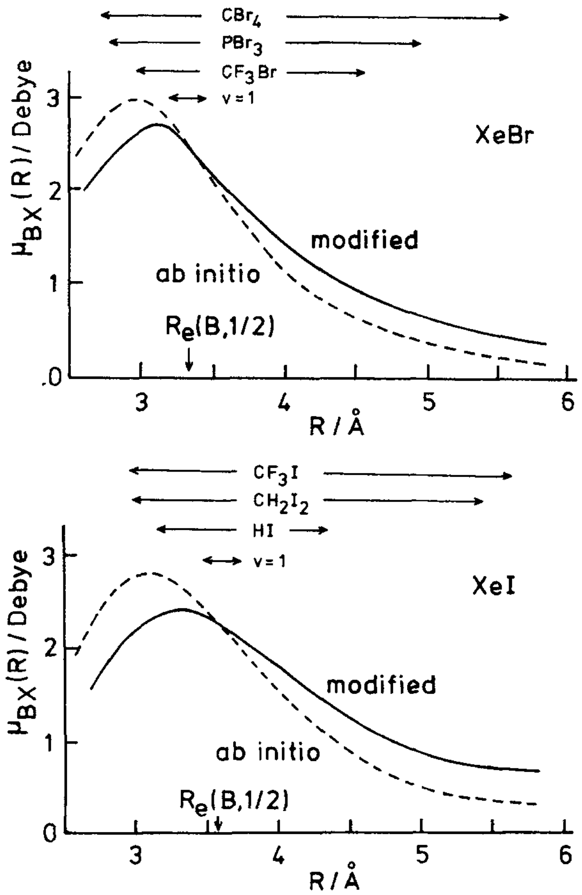

FIG. 8. Transition moment function, *ab initio* --- and modified — for XeBr(B–X) and XeI(B–X). The arrows indicate the range of internuclear distances that are applicable to the XeBr(B) or XeI(B) molecules formed by the various reactions. These transition moment functions give gradually declining Einstein coefficients with increasing v. The XeBr(XeI)A_v values (s^{-1}) are 8.2×10^7 (8.0×10^7) for $v=0$, 6.8×10^7 (6.2×10^7) for $v=40$, and 5.1×10^7 (4.4×10^7) for $v=100$.

the calculations are given in Table V. For XeI(B), $\omega_e' = 122\pm2$ cm^{-1} was found to be best for the Xe($^3P_2$)+HI spectrum and for the broad oscillatory structure in the low pressure CF$_3$I and CH$_2$I$_2$ spectra. The observed ω_e' values for XeBr(B) and XeI(B) are 9% and 12%, respectively, higher than the *ab initio* values. The easiest way to adjust the potentials to obtain better ω_e', without degrading the good relation found in the $\nu_A-\nu_B$ plot, is to simultaneously change the scale of the abscissa for both the upper and lower potential functions. Thus, the final potentials were expressed by Eqs. (6) and (7) with replacement of R by $1.09R$ and $1.12R$ for XeBr and XeI, respectively, and also substituting the values in parentheses of Table IV for T_e. These corrected XeBr and XeI potentials were used in the simulations to obtain the vibrational distributions.

The *ab initio* transition moments can be checked by comparing the calculated and experimental intensity envelopes. The *ab initio* transition moments were expressed as

$$\mu_{eg}^{HD}(R)=(c_0+c_1R+c_2R^2+c_3R^3+c_4R^4)^{-1} \tag{8}$$

by least-square fitting (see Table VI). Generally, the fit between the calculated and experimental spectra using the *ab initio* $\mu_{eg}^{HD}(R)$ was fairly good, although the calculated intensity of the long tail between ν_A and ν_B was too low by about a factor of 2. The defect in this region was removed by increasing the value of the transition moment at $R>R_e'$ relative to $R<R_e'$ by the following modification:

$$\mu_{eg}(R)=\exp[-\gamma(R-R_e')]\,\mu_{eg}^{HD}(R)\,, \tag{9}$$

with $\gamma=0.3$ and 0.4 for XeBr and XeI, respectively. The *ab initio* and best fit μ_{eg} are shown in Fig. 8.

TABLE VI. Transition moment coefficients.[a]

	Transition	c_0	c_1	c_2	c_3	c_4	γ
	B, 1/2–X, 1/2	33.50	−36.25	14.70	−2.648	0.182	0.3
XeBr	B, 1/2–A, 1/2	−11.02	12.03	−4.352	0.611	−0.022	
	C, 3/2–A, 3/2	19.96	−25.62	12.57	−2.799	0.248	
	B, 1/2–X, 1/2	20.95	−21.22	8.200	−1.430	0.098	0.4
XeI	B, 1/2–A, 1/2	2.74	−1.82	0.731	−0.189	0.023	
	C, 3/2–A, 3/2	23.48	−28.20	13.01	−2.731	0.228	

[a] To be used in Eqs. 8 and 9.

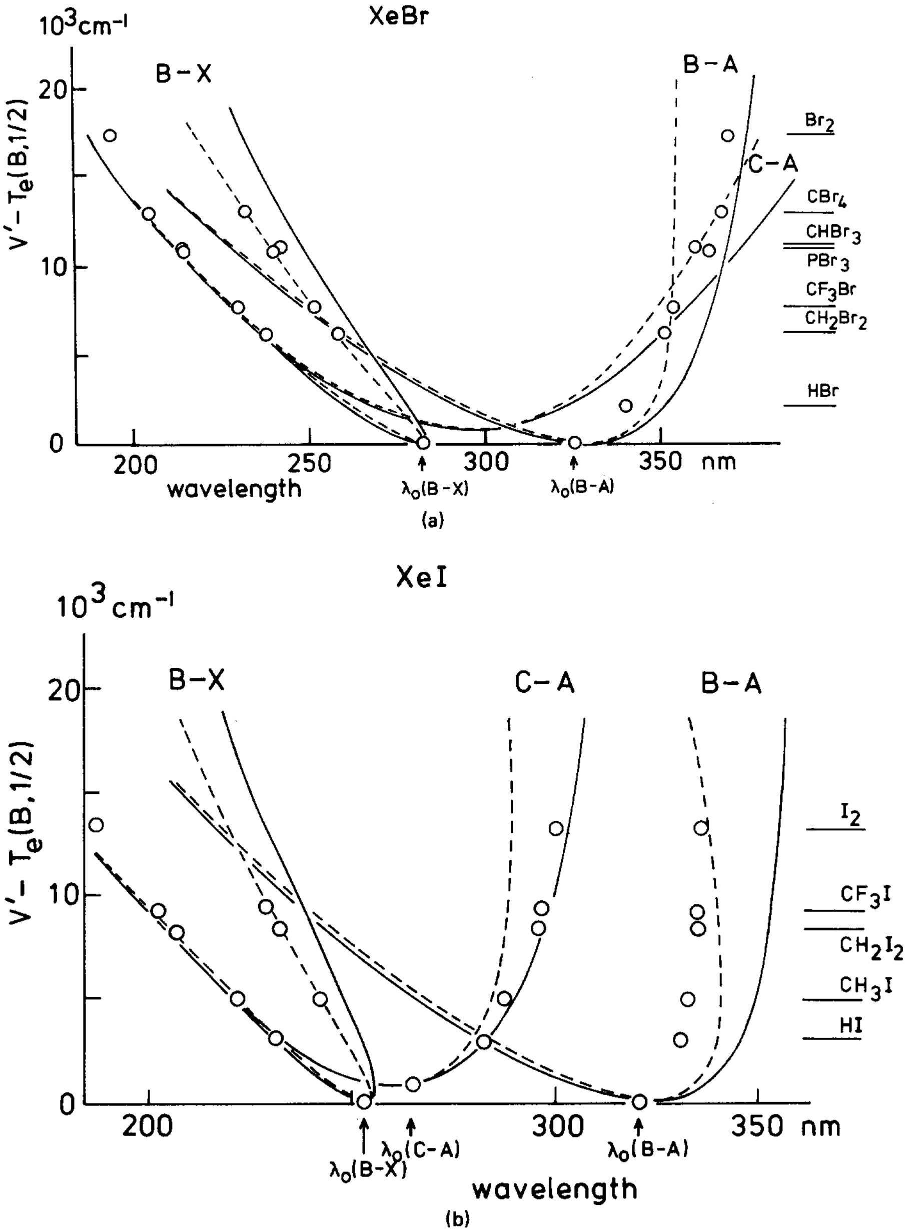

FIG. 9. Plot of $V'(R) - T_e$, which is the vibrational excitation, vs the wavelengths of the transitions at the classical turning points for XeBr and XeI. Curves are shown for the *ab initio* calculated curves — and for those curves adjusted for dispersion contributions - - -. The points are experimental assignments from Table IV; only transitions for the inner turning points are available for *B–A* and *C–A* bands. The horizontal lines to the right side of the figure indicate $E^{\text{obs}}_{V\max}$ for each reaction.

The broad 290–370 nm XeBr emission consists of $(B, 1/2\text{–}A, 1/2)$ and $(C, 3/2\text{–}A, 3/2)$ bands. The redmost peak shifts to shorter wavelength as the pressure is increased or as less exothermic reagents are used; the $(C\text{–}A)$ spectra of XeCl[4] and KrF[2] exhibit the same trend. The redmost peak roughly corresponds to ν_B of the inner turning point transition of the highest vibrational levels of B or C to $A(1/2, 3/2)$, since the repulsive potentials are very steep. Strictly speaking, there may be some ambiguity in the correspondence because of quantum mechanical spreading of the waves and contributions from lower vibrational levels. The λ_B in Table III were taken from the point where the intensity drops about 50% from the most intense, longest wavelength peak. Since the *C–A* emission is expected to be the most intense, these bands probably belong mainly to the *C–A* transition. Emission from low v levels is needed to assign the origin of the *C–A* and *B–A* transitions. The spectra from CBr$_4$, CHBr$_3$, and CF$_3$Br at ~50 Torr show one broad maximum at 325–335 nm. Above 100 Torr the Xe($^3P_1$) + CBr$_4$ spectra show a peak at 325 nm which may be assigned to the origin of the *B–A* transition.[8(c),8(d)] The origin of the *C–A* transition was not definitely determined but is < 320 nm. The spectra from HBr show more definite maxima at 322 and 335 nm, which are assigned to the *C–A* and *B–A* transitions, respectively.

Examination, in classical terms, of the band positions for a given vibrational energy for the *ab initio* potentials are useful for understanding the general features of the *B–A* and *C–A* spectra. Figure 9 shows the relations between vertical transitions from the turning points and the vibrational energy in the upper state. The ordinate is $E' = V'(R) - V[R_e(B \text{ or } C)]$ and the abscissa is $\nu = V'(R) - V''(R)$ or wavelength; the T_e values for the $(B, 1/2)$ state are those in parenthesis in Table III. The T_e values for $(C, 3/2)$ states also were changed by

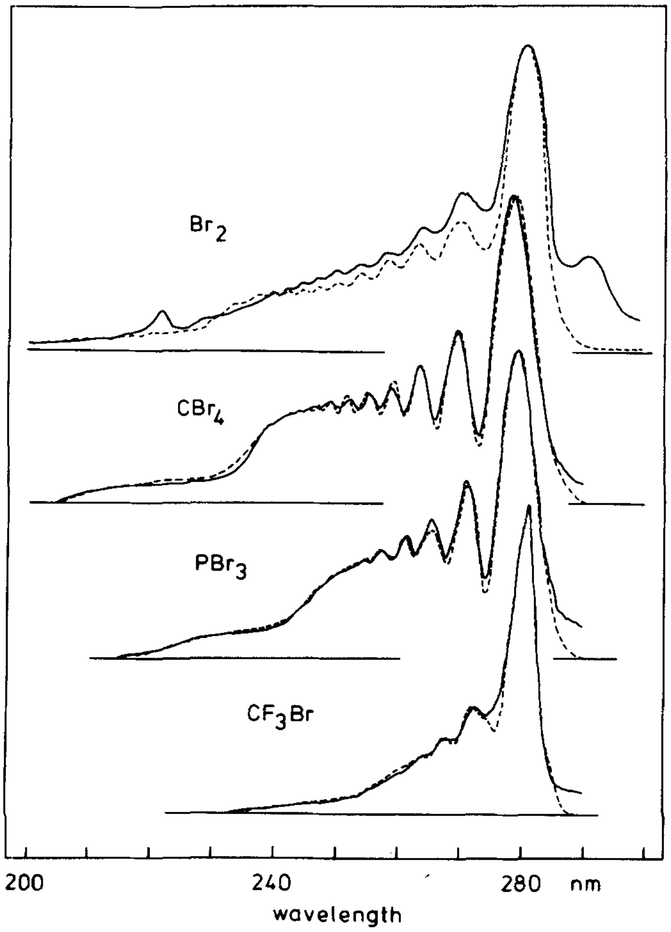

FIG. 10. Comparison of the experimental— and simulated - - - XeBr(B–X) chemiluminescence spectra from Br_2, CF_3Br, PBr_3, and CBr_4. The bump of the Br_2 spectrum at ~290 nm is a Br_2^* band. The experimental spectra were obtained at ≈ 0.2 Torr of Ar.

the same amount as for the (B, 1/2) states. As seen from Fig. 9, the XeBr(C–A) and XeBr(B–A) bands are completely overlapped except when the vibrational energy is very low. The calculated origin of the B–A band (329 nm) is reasonably close to the experimental estimate 325 nm but the calculated C–A band origin (298 nm) seems too low, even though the (C, 3/2) state was lowered by the same amount as for (B, 1/2). This observation is consistent with the need to have the *ab initio* C state energy lowered by more than the B state. However, this argument is not definitive because the experimental assignment of the XeBr(C–A) origin is still somewhat uncertain. The redmost bands observed for several reactions are indicated by open circles in Fig. 9; for reactions with modest vibrational energy they cannot be assigned uniquely to either B–A or C–A. Based upon the initial B/C ratio given in Table I and calculated[6] B–A/B–X branching fraction, the B–A transition contributes about 20% to the long wavelength emission intensity.

The B–A and C–A bands of XeI are almost completely separated. The redmost peak of the B–A band is located at almost the same position (335 nm) for I_2, CF_3I, and CH_2I_2 in spite of considerably different vibrational distributions. Increasing the pressure did not change the position of the redmost peak or even the deep oscillatory structure up to 8 Torr (see Fig. 2). Such behavior is expected if the slopes of the repulsive walls of the lower and upper states (case II in Ref. 2) are nearly identical. The curve from the dispersion corrected potentials in Fig. 9(b) is consistent with such behavior. The XeI(C–A) band is fairly sensitive to the vibrational distribution, although the oscillatory structure is not so large as for the B–A band, and the XeI(C–A) spectrum is therefore sensitive to pressure (see Fig. 2). Judging from vibrational energy dependence of the observed ν_B and the slope of the curve in Fig. 10(b), the dispersion correction was necessary, although our estimation might be too rough. The C–A and B–A band origins were determined from high pressure Xe($^3P_2$) + CF_3I spectra as 263 ± 3 and 320 ± 5 nm, respectively. The *ab initio* and the dispersion-corrected *ab initio* potentials both gave 260 and 323 nm, respectively.

The C–A and B–X transitions are well separated for XeF and XeCl but XeBr and XeI need more attention before a conclusion can be reached (see Fig. 9). We have theoretically estimated the overlap for B–X and C–A for XeI based on the *ab initio* transition moments. In the classical sense, the emission due to transition at nuclear distance R, i.e., $I(\nu)$, can be written[2] as

$$I(\nu) \propto \nu^3 P(R)\, \mu_{eg}(R)^2/(d\nu/dR)\ , \tag{10}$$

$$\nu = V'(R) - V''(R)\ , \tag{11}$$

$$P(R) = \int_{V'(R)}^{\infty} P(E)/[E - V'(R)]^{1/2}\, dE\ , \tag{12}$$

where $P(R)$ is the probability of finding a molecule with the internuclear distance between R and $R + dR$ for a particular vibration distribution $P(E)$. If more than one internuclear position gives the same frequency, Eq. (10) must be summed. The calculated classical spectrum showed excellent agreement with the quantum mechanically calculated spectrum for the same vibrational distribution, except for the absence of the oscillatory structure. The spectral region of XeI was divided into three domains at 258 and 300 nm (see Table VII). These regions correspond to the B–X, C–A, and B–A bands, respectively. The C–A emission falling into the B–X region is $\gtrsim$20% of the total C–A emission intensity. Although this value may be overestimated because of an incorrect T_e value for (C, 3/2) state, the overlapping probably is not negligible. According to Table VII, the amount of the overlapping seems to be insensitive to the

TABLE VII. XeI intensity distribution.

Transition	Reagent	($\lambda < 258$)[a]	($258 < \lambda < 300$)[b]	($300 < \lambda$)[c]
C–A	CF_3I	22	78	0
	CH_2I_2	24	76	0
	HI	24	76	0
B–A	CF_3I	10	29	60
	CH_2I_2	7	33	60
	HI	0	7	93

[a] Nominally corresponds to the B–X spectral region.
[b] Nominally corresponds to the C–A spectral region.
[c] Nominally corresponds to the B–A spectral region.

vibrational distribution, which is counter to intuitive thinking since the transition moment weights against transitions at larger R. The high pressure XeI spectra from Xe($^3P_1$)+CF_3I suggest that the overlap of the B–X and C–A bands is significant for a 300 K Boltzmann distribution.[8(c)] Although the B–X and C–A transitions from high v levels also may overlap somewhat, the appearance of the spectra (Fig. 5) suggests that it does not seriously affect the oscillatory behavior or the general shape of the B–X envelope. Since the B–X and C–A overlapping was ignored in compiling Table I, the B/C ratios may be somewhat too large.

C. Vibrational distributions from (B–X) simulations

The steady-state vibrational populations were fitted to flexible functions containing adjustable parameters. The functions utilized were the following:

(i) $P_V = (1 - f_V)^{3/2} \exp(-\lambda_V f_V)$,

(ii) $P_V = \exp[-\alpha(f_V - \bar{f}_V)^2]$,

(iii) P_V = a function expressed by a set of straight lines, such as a triangle, boxcar, or trapezoid,

(iv) P_V = linear combinations of these functions.

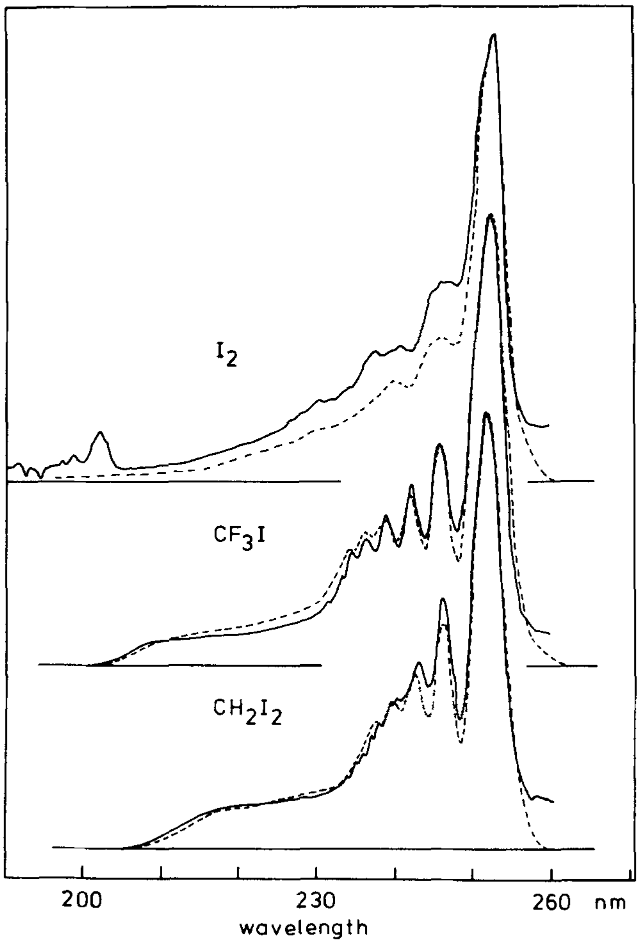

FIG. 11. Comparison of the experimental— and simulated - - - XeI(B–X) chemiluminescence spectra from CH_2I_2, CF_3I, and I_2. The experimental spectra were obtained at ≈ 0.2 Torr of Ar.

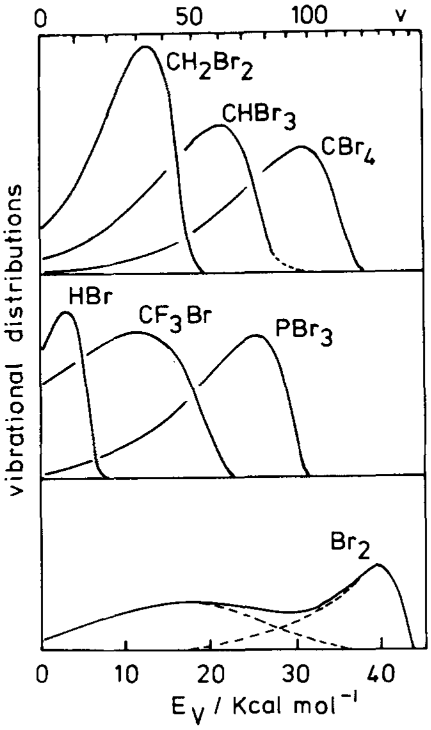

FIG. 12. XeBr(B) vibrational distributions used for the simulation of spectra shown in Fig. 10. The correspondence between E_V and vibrational level is shown by the scales at the top and bottom of the figure.

Case (i) is a linear surprisal distribution for a three body reaction. Strictly speaking Case (i) must be divided by the rotational constant B_V but this has been ignored. In using Case (i), f_V was defined as $E_V / E^{\text{obs}}_{V\max}$. We first used Case (i) and it was successful in some cases. Only when the simulated and the observed spectra were clearly impossible to fit by Case (i) were other functions used. The steady-state distributions can be converted to the initial distribution using the calculated Einstein coefficient (see the caption of Fig. 8), according to

$$P_V(\text{initial}) = A_V\, P_V(\text{steady state}) \; . \tag{13}$$

Comparisons of some simulated and experimental spectra are made in Figs. 10 and 11 and the vibrational distributions are shown in Figs. 12 and 13. A summary of $\langle E\rangle$, $E^{\text{obs}}_{V\max}$, $\langle E_V\rangle$, $\langle f_V\rangle$, and a description of the P_V are listed in Table VIII.

Bromine substitute methanes CH_nBr_{4-n} gave linear surprisal distributions with $\lambda_V = -8$, -6, -5, and $E^{\text{obs}}_{V\max}$ = 38.8, 31.5, and 19.0 kcal mol^{-1} for $n = 0$, 1, and 2, respectively; CH_3Br did not give significant XeBr emission even though $\langle E\rangle$ is 22.4 kcal mol^{-1}. The differences between $\langle E\rangle$ and $E^{\text{obs}}_{V\max}$ increase with the number of hydrogen. The decrease of λ_V for lower $E^{\text{obs}}_{V\max}$ results in the almost constant breadth of the distribution in this series. There is a slight difference between $E^{\text{obs}}_{V\max}$ and the $E^{\text{sim}}_{V\max}$ used in the simulation for $CHBr_3$. This was a matter of convenience because the simulated spectrum for a linear surprisal with $E^{\text{sim}}_{V\max}$ closely matched the experimental spectrum except for the extreme short λ tail. The modification of the surprisal distribution, indicated by the dotted extension of the distribution for $CHBr_3$ in Fig. 12, gives our best estimate of the true distribution. The PBr_3 and CF_3Br distributions were given by a linear sur-

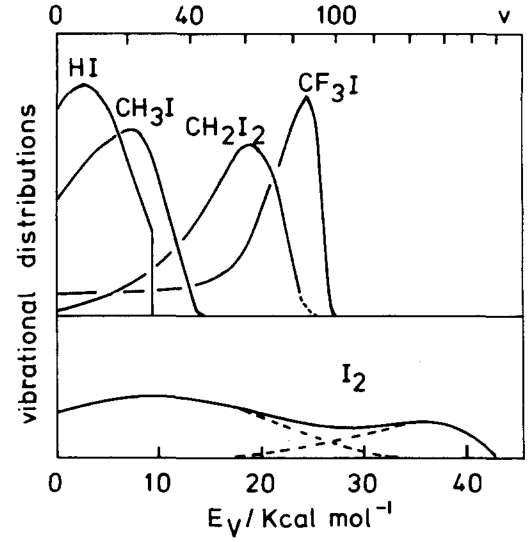

FIG. 13. XeI vibrational distributions used for the simulation of spectra shown in Fig. 11. The correspondence between E_V and vibrational level is shown by the two scales at the top and bottom of the figure.

prisal distribution with $\lambda_V = -7$ and -3, respectively. The PBr_3 distribution is similar to that of $CHBr_3$ and CBr_4. The broader distribution from CF_3Br relative to CH_2Br_2 is also supported by the XeBr(*C*, 3/2) emission since the *C*–*A* band at 290–360 nm is much broader than for CH_2Br_2. The available energy for the Br_2 reaction is the largest of the bromine donors, but the spectral features are very different from a simple extrapolation of the CH_nBr_{4-n} series. The oscillatory structure is shallow, although there are 10 maxima. The bimodal distribution of Fig. 12 is indeed very different from the other distributions and consists of a very sharp, high *v* component (0.36) plus a broad, low *v* component (0.64) that can be nearly expressed as a Gaussian, as shown in Fig. 12. We first tried to represent the vibrational distribution as a sum of two linear surprisal distributions, but a Gaussian type distribution was found to be better for the lower vibrational energy component.

The CH_2I_2 distribution is given by a linear surprisal with $\lambda_V = -7$ for $E^{\text{sim}}_{V\max} = 24.1$ kcal mol^{-1}. This distribution provides a good fit to the spectra except for the short wavelength region. The estimated best distribution is shown by the dotted extension to higher energy in Fig. 13. The $E^{\text{obs}}_{V\max}$ for CH_3I is smaller than $\langle E\rangle$ by 9.6 kcal mol^{-1}; but a linear surprisal distribution with $\lambda_V = -3.0$ (for $E^{\text{obs}}_{V\max} = 14.1$ kcal mol^{-1}) gives a satisfactory fit to the spectra. In order to fit the CF_3I spectrum, a very highly peaked distribution plus a broad component is required and satisfactory overall fit was obtained with a 50% flat distribution + 50% linear surprisal ($\lambda_V = -10$). Although $\langle E\rangle$ is nearly the same for CH_2I_2 and CF_3I, the distributions must differ significantly to fit the two spectra (see Fig. 11). The reduction in $\langle f_V\rangle$ and in $E^{\text{obs}}_{V\max}$ for CH_2I_2 and CH_3I parallels the systematic changes found for the CH_nBr_{4-n} series.

The XeI from I_2 is clearly much less excited than from CH_2I_2 or CF_3I and, in fact, the distribution resembles that for Br_2. The vibrational distribution has two distinct maxima with the contribution of the Gaussian component at low *v* being almost fives times larger than the linear surprisal distribution at higher *v*. The simulations for Br_2 and I_2 do not fit the experimental spectra as well as for the other reagents because it is difficult to find suitable functions for such abnormal distributions

TABLE VIII. Vibrational energy disposal for Xe($^3P_2$) with RBr and RI.

Reagent	$\langle E\rangle$[a] (kcal mol^{-1})	$E^{\text{obs}}_{V\max}$ (kcal mol^{-1})	$\langle E_V\rangle$ (kcal mol^{-1})	$\langle f_V\rangle$		Shape of the distribution[e]
CBr_4	42.4	38.8	27.8	0.66[b]	(0.72)[c]	$\lambda_V = -8.0$
$CHBr_3$	~35	31.5	17.7	0.50	(0.56)	$\lambda_V = -6.0 (E^{\text{sim}}_{V\max} = 27.9)$[f]
CH_2Br_2	30.4	19.0	10.9	0.36	(0.57)	$\lambda_V = -5.0$
CH_3Br	22.4	no XeBr emission				
CF_3Br	22.7	23.3	11.0	0.48	(0.47)	$\lambda_V = -3.0$
PBr_3	···	30.9	20.9	···	(0.68)	$\lambda_V = -7.0$
HBr	4.5	6.6	3.1	0.69	(0.47)	$\lambda_V = -3.0$
Br_2	45.6	45.3	25.6	0.56	(0.57)	1.0 ($\lambda_V = -15$) + 1.8 (Gaussian)
	35.1[d]			(see text)		
CH_3I	23.7	14.1	6.6	0.28	(0.47)	$\lambda_V = -3.0$
CF_3I	26.2	27.4	18.5	0.70	(0.67)	1.0 ($\lambda_V = -10$) + 0.5 flat
CH_2I_2	29.1	25.4	16.3	0.56	(0.64)	$\lambda_V = -7.0$ ($E^{\text{sim}}_{V\max} = 24.1$)[f]
HI	8.7	8.8	4.0	0.46	(0.45)	truncated Gaussian
I_2	43.5	43.5	20.0	0.46	(0.46)	1.0 ($\lambda_V = -10$) + 5.0 (Gaussian)
	21.4[d]			(see text)		

[a] $\langle E\rangle$ is the mean available energy and is the same as $E^{\text{ther}}_{V\max}$ of Table II. $E^{\text{obs}}_{V\max}$, from Table II, was used to calculate P_V in the linear surprisal equation.

[b] $\langle E_V\rangle/\langle E\rangle$; $\langle E_V\rangle$ was calculated from the steady-state distributions.

[c] $\langle E_V\rangle/E^{\text{obs}}_{V\max}$; $\langle E_V\rangle$ was calculated from the steady-state distributions.

[d] For formation of excited halogen atoms.

[e] In calculating the distribution from a given λ_V, the $E^{\text{obs}}_{V\max}$, rather than $\langle E\rangle$, was used to define f_V.

[f] $E^{\text{sim}}_{V\max}$ = maximum energy used in the simulation which differs from $E^{\text{obs}}_{V\max}$ for these two cases for convenience of using linear surprisal distribution in the simulation (see text).

and also because of the poorer reliability of the calculated basis spectra for transitions from the very high, $v>100$, vibrational levels.

The HBr and HI spectra show a series of almost equally spaced fine structure rather close to the main $B-X$ band. Unlike the broad oscillations in other spectra, each peak corresponds to an A-type transition from the outer turning point of each v' level (see Fig. 7). The positions of these peaks previously were used for checking the potentials. The reliability of the calculated intensities for the sharp A-type peaks may not be very good because of the rather wide sampling interval of frequency in the calculation and because of the overlapping of the background B-type transitions, which greatly depends on the repulsive character of the lower potential. Nevertheless, the population of mid v levels of XeBr or XeI must be favored over the very low v levels. The XeBr and XeI vibrational distributions are in qualitative agreement with the ArBr distribution,[9] which in turn was consistent with energy disposal to KBr from K + HBr. An additional possible problem for simulation of HBr and HI spectra is the expected high rotational excitation. Because of the light mass of the H atom, most of the initial orbital angular momentum of the collision will be released as product XeBr or XeI rotational angular momentum. This large rotational energy may ultimately require incorporation into the simulation model to obtain refined vibrational distributions.

V. DISCUSSION

A. Reaction dynamics for Br_2, I_2, and other halogens

The reactive cross sections for alkali metal and excited rare gas atoms with halogen molecules are comparable. Since Γ_{RgX} is ~1.0, the overall features of the alkali and alkaline earth metal and rare gas atom reactions with X_2 are in close correspondence,[7,18,19] and we now wish to compare the vibrational energy disposal patterns. The bimodal vibrational distributions from $Xe^* + Br_2$ and I_2 suggest exit channels corresponding to the formation of both ground and excited state halogen atoms

$$Xe^* + Br_2 \rightarrow XeBr(B,\ 1/2;\ C,\ 3/4) + Br(^2P_{3/2}) + 44.1\ \text{kcal mol}^{-1}\ , \tag{13a}$$

$$\rightarrow XeBr(B,\ 1/2;\ C,\ 3/2) + Br(^2P_{1/2})^* + 33.6\ \text{kcal mol}^{-1}\ , \tag{13b}$$

$$Xe^* + I_2 \rightarrow XeI(B,\ 1/2;\ C,\ 3/2) + I(^2P_{3/2}) + 42.1\ \text{kcal mol}^{-1}\ , \tag{14a}$$

$$\rightarrow XeI(B,\ 1/2;\ C,\ 3/2) + I(^2P_{1/2})^* + 20.4\ \text{kcal mol}^{-1}\ . \tag{14b}$$

Pronounced bimodal character was not found for $Xe^* + Cl_2$ or $+ F_2$; however, the sum of a flat and a linear surprisal distribution (from high v component) was required to simulate the XeF* and XeCl* spectra. The vibrational distributions for the halogen series are shown in Fig. 14; the $\langle f_V\rangle$ values decline as 0.72, 0.77, 0.63, and 0.45 from F_2 to I_2. If the flat component for XeCl* and XeF* is associated with excited Cl or F atom formation, the estimated branching fractions are 0.1, 0.3, 1.8, and 5.0 and there is a drastic enhancement in k^*/k for the heavier halogens. Since the spin–orbit interaction energies for Cl and F are small, the excited atom component is more difficult to assign and those k^*/k values are known with less reliability. If the two components of the Br_2 and I_2 distributions are associated with the two halogen spin–orbit states and if $\langle f_V\rangle$ is calculated separately for the two channels, the results become $\langle f_V\rangle_{Br} \cong 0.75$, $\langle f_V\rangle_{Br^*} \cong 0.55$, $\langle f_V\rangle_{I} \cong 0.70$, and $\langle f_V\rangle_{I^*} \cong 0.50$. The lower spin–orbit channel closely resembles the results for F_2 or Cl_2; however, the upper spin–orbit channel definitely has lower vibrational energy disposal. In addition to the spin–orbit halogen states, two rare gas halide states also are formed so there are actually four exit channels. Since both XeX(B) and XeX(C) appear to have the same vibrational distribution, there is no strong evidence for coupling between the two pairs of states.

The translational distributions[20,21] for $K + I_2$ and Br_2 are relatively broad, but $\langle f_T\rangle$ is only ~0.07. The $Li + Cl_2$ and Br_2 reactions[22] also have broad translational distributions and $\langle f_T\rangle$ is higher (~0.22). Some, but not all, of these translational distributions show coupling with scattering angle. The increase in $\langle f_T\rangle$ from $\lesssim 0.1$ for K, Rb, and Cs to ~0.2 for Li seems established,[10]

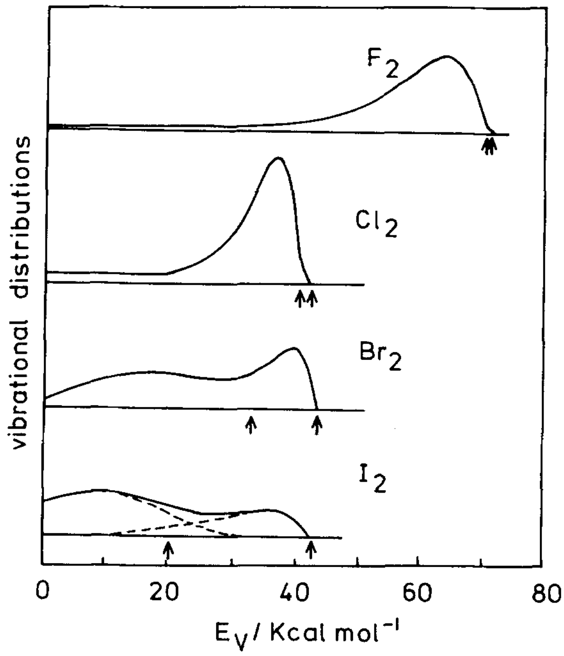

FIG. 14. Comparison of the XeX* vibrational distributions from the $Xe(^3P_2) + X_2$ reactions. The arrows indicate the energy limit for the formation of $X(^2P_{3/2})$ and $X(^2P_{1/2})$ states. The XeCl* and XeF* results were taken from Ref. 3.

but for comparison with Xe* atom reactions $\langle f_T \rangle \approx 0.1$ seems appropriate. The $\langle f_R \rangle$ for $M + X_2$ is less certain,[10] but recommended values seem to be $\lesssim 0.1$. Thus, for alkali metal atom reactions the $\langle f_V \rangle$ values are 0.8–0.7, which is in the same range as for the $XeX + X(^2P_{3/2})$ channel. Using surprisal analysis, Levine and Bernstein[23] showed that KI translational distribution from $K + I_2$ could be expressed as the sum of two linear surprisal distributions. They suggested these might correspond to I and I* channels. On the other hand, there is no systematic variation in $\langle f_T \rangle$, when computed with full exoergicity of the reaction, for the $M + Cl_2$, Br_2, I_2 series. Based on the MX translational distributions, there is no compelling reason to conclude that formation of X* is important for $M + X_2$. Rommel and Schultz[24(b)] found an unusually broad CaCl vibrational distribution from $Ca + Cl_2$ compared to reagents such as CCl_4, $CFCl_3$, and CF_2Cl_2. A similar trend, but less extreme in nature, was observed for $Xe^* + Cl_2$ and CCl_4. The CaBr and CaI distributions from $Ca + Br_2$ and I_2 have not been reported.

Without doubt, the vibrational energy disposal for $Xe(^3P_2)$ and $Xe(^3P_1)$ reacting with Br_2 or I_2 differs significantly from that of the corresponding alkali metal atom reactions. The $Kr(^3P_2) + X_2$ reactions show[7,25] the same trend in $\langle f_V \rangle$ as the $Xe(^3P_2)$ atom reactions, so this conclusion also holds for $Kr(^3P_2)$ atom reactions. We believe that the explanation of the difference between alkali metal atoms and rare gas atoms is the increasing importance of the $X(^2P_{1/2})$ exit channel as the halogen becomes heavier for the rare gas atom $+ X_2$ reactions. If this is the explanation, the excited $X_2^-(^2\Pi_g)$ states are likely to be more involved for the rare gas* $+ X_2$ reactions than for the metal atom $+ X_2$ reactions. We previously have argued for the importance of the $X_2^-(^2\Pi_g)$ state based upon simple correlation arguments for forming $XeCl(B) + Cl(^2P_{3/2})$ and $XeCl(C) + Cl(^2P_{3/2})$ from $Xe(^3P_2) + X_2$. The argument is much stronger now because both $X(^2P_{3/2})$ and $X(^2P_{1/2})$, as well as $XeX(B)$ and $XeX(C)$, seem to be product channels. The schematic potential diagram shown in Fig. 15 summarizes this viewpoint. The major question is how do the trajectories reach the excited anion potential and why does it become more important for the heavier halogens. The answer to the latter probably is related to the larger spin–orbit splitting in the $X_2^-(^2\Pi_g)$ state and the larger E.A. of this excited state for the heavier halogens.[30] There are two possibilities, both consistent with the orbiting model[5] of the quenching cross sections, for rationalizing how trajectories reach the $Xe^+, X_2^-(^2\Pi_g)$ potential: (i) The Xe^*, X_2 trajectories may pass through the $Xe^+, X_2^-(^2\Sigma_u^+)$ crossing and subsequently branch to the $Xe^+, X_2^-(^2\Pi_g)$ potential and (ii) trajectories that initially branch to the $Xe^+, X_2^-(^2\Sigma_u^+)$ pathway cross into the excited ion potential during subsequent motions on the lower potential. The fact that X_2^{-*} formation from trajectories that sample the $Xe^+, X_2^-(^2\Sigma_u^+)$ potential competes[7,19] with $XeX^* + X$ formation shows that coupling between the X_2^- and $(X_2^-)^*$ potential could be possible. Resolution of the problem requires more knowledge of the X_2^- and $(X_2^-)^*$ potentials. Strongly held but differing opinions about the vertical electron affinities of halogens are held by groups studying electron attachment and photodetachment[31,25] and by groups doing dynamical studies.[30,26] Until the isolated X_2^- potential curves are understood, little progress can be expected on more complicated issues involving these states.

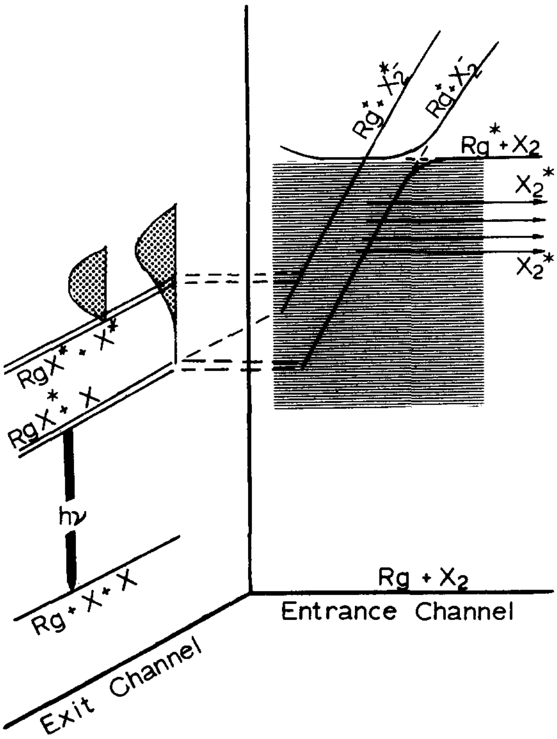

FIG. 15. Schematic representation of the role that $X_2^-(^3\Sigma_u^+)$ and $X_2^-(^2\Pi_g)$ potentials may play in the reaction of $Xe(^3P_2)$ and $Xe(^3P_1)$ atoms with X_2 forming $XeX(B,C) + X(^2P_{3/2})$ and $XeX(B,C) + X(^2P_{1/2})$. The shaded areas represents the quasicontinuum of X_2^{-*} states. The $Xe(^3P_0)$ and $Xe(^1P_1)$ potentials, which correlate to $XeX(D) + X$ via $Xe^+(^2P_{1/2}) + X_2^-$, are not shown.

In conclusion, the $Xe(^3P_{2,1})$ atom reactions with molecular halogens do differ from alkali metal atom reactions in energy disposal and this is ascribed to the greater involvement of the $(X_2^-)^*$ potential during the course of the excited state rare gas atom reactions.

B. Vibrational energy disposal for polyatomic reagents

The XeBr and XeI vibrational distributions may be compared to the BaBr and BaI distributions for the halogentated methane series of reagents. The comparison in Table IX illustrates that $\langle f_V(BaX) \rangle$ is larger than for $\langle f_V(XeX) \rangle$ for every case except CH_2I_2. In each case the metal halide distribution is considerably more narrow and frequently is described as bell shaped, whereas the XeX distributions are more nearly linear surprisal type distributions. For the revised $D_0(BaX)$,[29] which have been used in Table IX, the BaBr distributions from CBr_4 and $CHBr_3$ actually extend above the thermochemical limit. However, even if the experimental data should require slight revision, the difference between the XeX and BaX distributions would persist. The energy disposal to YbX[32] seems to parallel that for XeX; however, the available energy is much smaller and this comparison will not be pursued further.

TABLE IX. Comparison of energy disposal in Xe($^3P_2$) and Ba + CH_nX_{4-n} reactions.

Reaction	$\langle E \rangle$ (kcal/mol)	$\langle E \rangle - E_{V\max}^{\mathrm{obs}}$ (kcal/mol)	$\langle E_V \rangle / \langle E \rangle$	$\Delta E_{1/2}$[f] (kcal/mol^{-1})
Xe($^3P_2$) + CBr_4	42.4	3.6	0.66	12
$CHBr_3$	35	3.5	0.50	12
CH_2Br_2	30.4	11.4	0.36	10
CH_3Br	22.4	a		
CH_2I_2	29.2	3.6	0.56	11
CH_3I	23.7	9.5	0.28	11.5
Ba + CBr_4[c]	38.3[b]	−1.7	0.94	7.6
$CHBr_3$[c]	31.8[b]	−0.6	0.87	8.0
CH_2Br_2[c]	26.3[b]	4.2	0.53	7.8
CH_3Br[c,d]	18.3[b]	3.2	0.30(0.35)[d]	8.3
CH_2I_2[e]	28[b]	7.8	0.56	5.6
CH_3I[e]	20[b]	5.5	0.40	7.7

[a] No XeBr emission was observed from this reaction.

[b] Adjusted for improved values of D_0 (BaBr) and D_0 (BaI) from Ref. 29.

[c] From Ref. 24.

[d] From Ref. 28.

[e] From Ref. 14.

[f] Width of the distribution at half maximum.

The comparison in Table IX includes molecules with very low Γ_{XeX} such as CH_3I and CH_2Br_2 and molecules with $\Gamma_{\mathrm{XeX}} \gtrsim 0.1$ such as CH_2I_2, $CHBr_3$, and CBr_4. The low Γ_{XeX} reagents have small E.A. and slow electron attachment rates and metal atom reactions with these reagents give backwards or sideways reactive scattering. The reagents with higher Γ_{XeX} dissociatively attach thermal electrons with high rates and give forward reactive scattering with metal atom. For both metal and xenon atom reactions the trend of increasing $\langle f_V \rangle$ or decreasing $\langle f_T \rangle$ with increasing degree of halogenation is qualitatively consistent with the scattering data and with expectations about the nature of the halogenated methane ion.[33] For rebound reactions [which include those reagents giving low $\langle f_V(\mathrm{XeX}) \rangle$], the constraint associated with recoil momentum is the most important feature of the energy disposal and the energy released to the polyatomic group is of lesser importance.[34] Although the trends in $\langle f_V \rangle$ are similar for Xe($^3P_2$) and Ba atom reactions, there is a significant absolute difference in vibrational energy disposal. Since the available data suggest that the energy disposal for reactions of alkali and alkaline earth atoms are similar,[10] it follows that the energy disposal for the Xe($^3P_2$) reactions in Table IX differs from the corresponding alkali metal atom reactions too. The entrance to the Coulombic part of the potential surface should be the same for alkali metal and Xe atoms. We suggest that the systematic difference between $\langle f_V(\mathrm{MX}) \rangle$ and $\langle f_V(\mathrm{XeX}) \rangle$ may be associated with the low Γ_{XeX}, i.e., only a small fraction of the trajectories that enter the potential surface actually traverse the full Coulombic potential to yield XeX + R. In contrast, all of the metal atom reactive events yield MX + R. If this is the explanation, then selective loss of trajectories that normally would give highly vibrationally excited XeX must occur. This seems plausible because the trajectories with *high* (*vibrational*) *excitation* in the Xe^+–XR^- coordinate will sample *more of the surface* and spend a *longer time* on the surface than an event with *high* (*translational*) *energy* in the Xe^+–XR^- coordinate. This suggestion is by no means proven and numerous other possibilities, such as the role of different ionization energy of the alkaline earth metal atoms, may ultimately prove to be important. In closing this section we note that the XeCl distribution[3] from CCl_4 and the XeBr distribution from CBr_4 are virtually the same with $\langle f_V \rangle = 0.65$. The BaCl and CaCl distributions[24(b),35] from CCl_4 resemble each other with $\langle f_V \rangle \approx 0.75$, but these distributions are considerably narrower than the XeCl distribution. The Ba + CBr_4 reaction seems to be anomalous with a sharply peaked BaBr vibrational distribution with $\langle f_V \rangle = 0.94$. The most recent molecular beam report[36] shows a strong coupling between E_T' and scattering angle in the Cs, Rb, K + CCl_4 series. Visual estimates of the Cs and Rb data[36] suggest $\langle f_T \rangle \approx 0.15$.

The CF_3X series merits a separate discussion. For CF_4 and CF_3Cl, Γ_{XeX} is insignificant as expected from the slow rate of attachment of thermal electrons.[37] However Γ_{XeX} increases to 0.14 and 0.38 for CF_3Br and CF_3I, which have larger E.A. values and readily attach thermal electrons.[38] An increase in $\langle f_V(\mathrm{XeX}) \rangle$ from 0.48 to 0.70 also is observed for these two reagents. The $\langle f_V(\mathrm{BaX}) \rangle$ values for Ba + CF_3Br[27] and CF_3I[39] are $\gtrsim 0.85$ but the detailed shapes of the distributions are not yet available. The first interpretation of the BaI data has been revised and the distribution is unimodal peaking at high $\langle f_V \rangle$.[39(b)] The qualitative agreement between $\langle f_V(\mathrm{XeI}) \rangle$ and $\langle f_V(\mathrm{BaI}) \rangle$ from CF_3I lends some support to the explanation above, which associated with difference in BaX and XeX energy disposal with low Γ_{XeX}. Translational energy disposal[34] and variation of reaction probability with orientation[40] have been actively studied for K + CF_3I. There is a modest degree of coupling between E_T' and scattering angle and $\langle f_T(\mathrm{KI}) \rangle = 0.28$. This coupling probably is related to the propensity for the "heads" approach to give backward scattering while the "tails" approach gives forward scattering [but see, also, Ref. 40(d)]. The $\langle f_T(\mathrm{KI})\rangle$ is in good correspondence with $1.0-\langle f_V(\mathrm{XeI})\rangle$. The apparent two component (but not bimodal) XeI distribution may be associated with coupling of energy disposal and orientation of CF_3I in the collision with Xe*. Trifluoromethyl iodide anion has been observed by ESR spectroscopy.[41] The dissociation energy of CF_3I^- is ~10 kcal mol^{-1} and the electron is in an $a_1(\sigma^*)$ orbital that is located between the carbon and iodine atoms. The significant spin (electron) density[41] on the carbon atom may help to explain why reaction occurs for "sideways"[40(d)] and tails orientation, as well as for the intuitively more favorable heads configurations.

VI. CONCLUSIONS

The XeI and XeBr chemiluminescence from the reactions of Xe($^3P_2$) and Xe($^3P_1$) atoms with a series of iodide and bromide donors has been recorded. In each case, both the (B, 1/2) and (C, 3/2) states are formed. Potential curves for XeI(X, A, B, C) and XeBr(X, A, B, C) states were developed using the *ab initio* curves as a starting point. These refined potential curves were used to simulate the low pressure XeBr(B–X) and XeI(B–X) spectra and to estimate the XeBr(B) and XeI(B) vibrational distributions. The vibrational energy disposal was discussed in terms of the covalent–ionic curve crossing mechanism and the nature of the anion. For the molecular halogens $\langle f_V(\mathrm{XeX})\rangle$ declines as the atomic number of the halogen increased. This is attributed to the increasing importance of the upper spin–orbit state X($^2P_{1/2}$) as a product channel. This trend is not apparent in the reactions of alkali metal atoms with halogens. A close correspondence of $\langle f_V\rangle$ is found between Xe($^3P_2$) and K or Ba with CF_3I and between Xe($^3P_2$) and Ba with CH_2I_2. However, $\langle f_V(\mathrm{XeBr})\rangle$ is lower than $\langle f_V(\mathrm{BaBr})\rangle$ and the XeBr distributions are broader from the CH_nBr_{4-n} series and from CH_3I. This difference between Xe($^3P_2$) and Ba atom reactions may be associated with multiple potentials in the exit channel for Xe* reactions which result in low Γ_{XeX} and selective loss of trajectories favoring high $f_V(\mathrm{XeX})$. On the other hand, Simons and co-workers[42] have shown that the degree of rotational alignment of the XeX* products closely parallels the behavior of alkali metal atom reactions in spite of low Γ_{XeX} and multiple curve crossings. Thus, the final explanation of the differences in energy disposal for Xe* and Ba atom reactions with CH_3I and CH_nBr_{4-n} must await further tests.

ACKNOWLEDGMENTS

This work at Kansas State University was supported by the National Science Foundation and by the U.S. Department of Energy. We thank Trecil Dreiling (Kansas State University) for assistance in collection of some data and for carefully reading the manuscript. We also thank Professor J. P. Simons for a preprint of Ref. 42.

---

[1] J. E. Velazco, J. H. Kolts, and D. W. Setser, J. Chem. Phys. **65**, 3468 (1976).
[2] K. Tamagake and D. W. Setser, J. Chem. Phys. **67**, 4370 (1977).
[3] J. H. Kolts, J. E. Velazco, and D. W. Setser, J. Chem. Phys. **71**, 1247 (1979).
[4] K. Tamagake, J. H. Kolts, and D. W. Setser, J. Chem. Phys. **71**, 1264 (1979).
[5] J. E. Velazco, J. H. Kolts, and D. W. Setser, J. Chem. Phys. **69**, 4357 (1978).
[6] P. J. Hay and T. H. Dunning, J. Chem. Phys. **69**, 2209 (1978).
[7] D. W. Setser, T. D. Dreiling, H. C. Brashears, Jr., and J. H. Kolts, Faraday Discuss. Chem. Soc. **67**, 255 (1979).
[8] (a) H. C. Brashears Jr., and D. W. Setser, J. Phys. Chem. **84**, 224 (1980); (b) J. H. Kolts and D. W. Setser, J. Phys. Chem. **82**, 1766 (1978). The XeF results in Fig. 2 are incorrect. Proper accounting of background emission alters the B/C ratio for XeF such that it closely matches the curve shown for KrF. The extrapolated high pressure C/B ratios given in this paper give false limits; see Ref. 8(a); (c) H. C. Brashears Jr., Y. C. Yu, and D. W. Setser (to be published); (d) J. Tellinghuisen and M. R. McKeever, Chem. Phys. Lett. **72**, 94 (1980).
[9] M. F. Golde and A. Kvaran, J. Chem. Phys. **72**, 434, 442 (1980).
[10] B. E. Holmes and D. W. Setser, "Energy Disposal in Chemical Reactions," in *Physical Chemistry of Fast Reactions*, edited by I. W. M. Smith, (Plenum, New York, 1980), Vol. 3.
[11] P. J. Marcoux, M. van Swaay, and D. W. Setser, J. Phys. Chem. **83**, 3168 (1979).
[12] B. de Darwent, "Bond Dissociation Energies in Simple Molecules," Natl. Stand. Ref. Data Ser. Natl. Bur. Stand. **31** (1970).
[13] D. R. Stull and H. Prophet, "JANAF Thermochemical Tables," Natl. Stand. Ref. Data Ser. Natl. Bur. Stand. **37** (1971).
[14] P. J. Dagdigian, H. W. Cruse, and R. N. Zare, Chem. Phys. **15**, 249 (1976).
[15] E. H. Okafo and E. Whittle, J. Chem. Soc. Faraday Trans. 1 70, 1366 (1974).
[16] M. Bourne and LeCalve, J. Chem. Phys. **58**, 1452 (1973).
[17] (a) J. Tellinghuisen, A. K. Hays, J. M. Hoffman, and G. C. Tisone, J. Chem. Phys. **65**, 4473 (1976); (b) J. Tellinghuisen (private communication, 1980).
[18] C. T. Rettner and J. P. Simons, Faraday Discuss. Chem. Soc. **67**, 329 (1979).
[19] R. J. Hennessy and J. P. Simons, Chem. Phys. Lett. **75**, 43 (1980).
[20] K. T. Gillen, A. M. Rulis, and R. B. Bernstein, J. Chem. Phys. **54**, 2831 (1971).
[21] T. T. Warnock, R. B. Bernstein, and A. E. Grosser, J. Chem. Phys. **46**, 1685 (1967).
[22] C. M. Sholeen, L. A. Gundel, and R. R. Herm, J. Chem. Phys. **65**, 3223 (1976).
[23] R. B. Bernstein and R. D. Levine, Adv. At. Mol. Phys. **11**, 253 (Fig. 19) (1975).
[24] (a) M. Rommel and A. Schultz, Ber. Bunsenges. Phys. Chem. **81**, 139 (1977); (b) A. Schultz (private communication, 1980).
[25] J. H. Kolts, Ph.D. thesis, Kansas State University (1978).
[26] (a) W-C. Tam and S. F. Wang, J. Chem. Phys. **68**, 5627 (1978); (b) L. C. Lee, G. P. Smith, J. T. Moseley, P. C. Gosby, and J. A. Guest, J. Chem. Phys. **70**, 3237 (1979).
[27] The location of the $Cl_2^-(^2\Sigma_u^+)$ and $Cl_2^-[^2\Pi_g(1/2)]$ curves is still subject to controversy; see Refs. 25(a), 25(b), and 7 and E. A. Gislason, in *Alkali Halide Vapors, Structural, Spectra and Reaction Dynamics*, edited by P. Davidovits and D. C. McFadden (Academic, New York, 1979).
[28] R. W. Solarz and S. A. Johnson, J. Chem. Phys. **70**, 3592 (1979).
[29] (a) D. L. Hildenbrand, J. Chem. Phys. **66**, 3526 (1977); (b) P. D. Kleinschmidt and D. L. Hildenbrand, *ibid*. **68**, 2823 (1978).
[30] M. Kimura and K. Lagmann, J. Chem. Phys. **69**, 4938 (1978).

[31] H. L. Brooks, S. R. Hunter, and K. J. Nygaard, J. Chem. Phys. **71**, 1870 (1979).

[32] R. Dirscherl and H. U. Lee, J. Chem. Phys. **73**, 3831 (1980).

[33] (a) W. E. Wentworth, R. George, and H. Keith, J. Chem. Phys. **51**, 1791 (1969); (b) E. Schultes, A. A. Christodoulides, and R. N. Schindler, Chem. Phys. **8**, 354 (1975).

[34] R. B. Bernstein and B. E. Wilcomb, J. Chem. Phys. **67**, 5809 (1977).

[35] W. Schmidt, A. Siegel, and D. Schultz, Chem. Phys. **16**, 161 (1976).

[36] S. J. Riley, P. E. Siska, and D. Herschbach, Faraday Discuss. Chem. Soc. **67**, 27 (1979).

[37] R. Schumacher, H. R. Sprunken, A. A. Christodoulides, and R. N. Schindler, J. Phys. Chem. **82**, 2248 (1978).

[38] (a) R. N. Compton, P. W. Reinhardt, and C. D. Cooper, J. Chem. Phys. **68**, 4360 (1978); (b) S. Y. Tang, B. P. Mathur, E. W. Rothe, and G. P. Reck, J. Chem. Phys. **64**, 1270 (1976).

[39] (a) G. P. Smith, J. C. Whitehead, and R. N. Zare, J. Chem. Phys. **67**, 4912 (1977); (b) J. Allison, M. A. Johnson, and R. N. Zare, Faraday Discuss. Chem. Soc. **67**, 324 (1979), and private communication.

[40] (a) P. R. Brooks, Faraday Discuss. Chem. Soc. **55**, 299 (1973); (b) G. Marcelin and P. R. Brooks, J. Am. Chem. Soc. **95**, 7885 (1973); (c) J. R. Hardee and P. R. Brooks, J. Phys. Chem. **81**, 1031 (1977); (d) P. R. Brooks, J. S. McKillop, and H. G. Pippin, Chem. Phys. Lett. **66**, 144 (1979).

[41] (a) A. Hasegawa, M. Shiotani, and F. Williams, Faraday Discuss. Chem. Soc. **63**, 157 (1977); (b) J. T. Wang and F. Williams, J. Am. Chem. Soc. **102**, 2860 (1980); (c) J. T. Wang and F. Williams, Chem. Phys. Lett. **72**, 557 (1980); (d) M. C. R. Symons, Chem. Phys. Lett. **72**, 559 (1980).

[42] R. J. Hennessy, Y. Ono, and J. P. Simons, J. Mol. Phys. (in press).